

A study in scarlet

II. Spectroscopic properties of a sample of intermediate-luminosity red transients

G. Valerin^{1,*}, A. Pastorello¹, E. Mason², A. Reguitti^{1,3}, S. Benetti¹, Y.-Z. Cai^{4,5,6}, T.-W. Chen⁷, D. Eappachen^{8,9}, N. Elias-Rosa^{1,10}, M. Fraser¹¹, A. Gangopadhyay^{12,13}, E. Y. Hsiao¹⁴, D. A. Howell^{15,16}, C. Inerra¹⁷, L. Izzo^{18,19}, J. Jencson²⁰, E. Kankare²¹, R. Kotak²¹, P. Lundqvist^{12,22}, P. A. Mazzali^{23,24}, K. Misra²⁵, G. Pignata²⁶, S. J. Prentice²⁷, D. J. Sand²⁸, S. J. Smartt^{29,30}, M. D. Stritzinger³¹, L. Tartaglia³², S. Valenti³³, J. P. Anderson^{34,35}, J. E. Andrews²⁸, R. C. Amaro²⁸, C. Barbarino¹², S. Brennan¹², F. Bufano³⁶, E. Callis¹², E. Cappellaro¹, R. Dastidar^{37,35}, M. Della Valle^{18,38}, A. Fiore^{1,39,40}, M. D. Fulton³⁰, L. Galbany^{10,41}, M. Gromadzki⁴², T. Heikkilä²¹, D. Hiramatsu^{14,15,43,44}, E. Karamahmetoglu^{12,31}, H. Kuncarayakti^{21,45}, G. Leloudas⁴⁶, M. Limongi^{47,48,49}, M. Lundquist²⁸, C. McCully¹⁵, T. E. Müller-Bravo^{10,41}, M. Nicholl³⁰, P. Ochner^{1,50}, E. Padilla Gonzalez^{15,16}, E. Paraskeva⁵¹, C. Pellegrino⁵², A. Rau⁵³, D. E. Reichart⁵⁴, T. M. Reynolds^{20,55,56}, R. Roy⁵⁷, I. Salmaso¹, M. Shahbandeh^{58,59}, M. Singh⁶⁰, J. Sollerman¹², M. Turatto¹, L. Tomasella¹, S. Wyatt²⁸, and D. R. Young³⁰

(Affiliations can be found after the references)

Received 31 July 2024 / Accepted 26 September 2024

ABSTRACT

Aims. We investigate the spectroscopic characteristics of intermediate-luminosity Red Transients (ILRTs), a class of elusive objects with peak luminosity between that of classical novae and standard supernovae. Our goal is to provide a stepping stone in the path to unveiling the physical origin of these events based on the analysis of the collected datasets.

Methods. We present the extensive optical and near-infrared (NIR) spectroscopic monitoring of four ILRTs, namely NGC 300 2008OT-1, AT 2019abn, AT 2019ahd and AT 2019udc. First we focus on the evolution of the most prominent spectral features observed in the low-resolution spectra. We then present a more detailed description of the high-resolution spectrum collected for NGC 300 2008OT-1 with the Very Large Telescope equipped with UVES. Finally, we describe our analysis of late-time spectra of NGC 300 2008OT-1 and AT 2019ahd through comparisons with both synthetic and observed spectra.

Results. Balmer and Ca lines dominate the optical spectra, revealing the presence of slowly moving circumstellar medium (CSM) around the objects. The line luminosity of H α , H β , and Ca II NIR triplet presents a double peaked evolution with time, possibly indicative of interaction between fast ejecta and the slow CSM. The high-resolution spectrum of NGC 300 2008OT-1 reveals a complex circumstellar environment, with the transient being surrounded by a slow (~ 30 km s⁻¹) progenitor wind. At late epochs, optical spectra of NGC 300 2008OT-1 and AT 2019ahd show broad (~ 2500 km s⁻¹) emission features at ~ 6170 Å and ~ 7000 Å which are unprecedented for ILRTs. We find that these lines originate most likely from the blending of several narrow lines, possibly of iron-peak elements.

Key words. circumstellar matter – supernovae: general – supernovae: individual: NGC 300 2008OT-1 – supernovae: individual: AT 2019abn – supernovae: individual: AT 2019ahd – supernovae: individual: AT 2019udc

1. Introduction

The transient sky is brimming with a wide variety of phenomena, and spectroscopic observations are a crucial tool for navigating through such a complex landscape. Indeed, remarkable efforts have been made in order to promptly classify newly discovered transients, culminating in the formation of dedicated spectroscopic surveys such as the “Public European Southern Observatory Spectroscopic Survey of Transient Objects” (PESSTO) consortium (Smartt et al. 2015). The swift collection of spectra is rewarded with key insights into the ongoing physical processes that could not be otherwise probed. In recent years, a growing number of studies have targeted objects displaying narrow and intense emission lines coupled with a

slow spectral evolution: these are the hallmarks of an optically thick circumstellar medium (CSM) surrounding the transient (e.g. Blinnikov 2017). This scenario has been investigated primarily in supernovae II_n (SNe II_n): terminal stellar explosions within an opaque CSM formed during the years prior to the event (Filippenko 1997). Critically, SNe II_n are not the only events showing evidence of optically thick CSM. The giant non-terminal eruptions of evolved massive stars, sometimes called giant luminous blue variables (LBVs) eruptions, mimic the characteristics of a genuine SN despite being non-terminal events: for this reason they earned the designation as ‘SN impostors’ (e.g. Van Dyk & Matheson 2012). The picture was further complicated by the discovery of other classes of transients that display clear signs of CSM in their spectra. Luminous red novae (LRNe) have been argued to arise from mergers of non-degenerate stars after a common-envelope

* Corresponding author; giorgio.valerin@inaf.it

phase where the final product of the merger event is expected to survive (Pastorello et al. 2019). Finally, there are the subjects of the present study, and perhaps the most poorly understood among the objects discussed so far: the intermediate-luminosity red transients (ILRTs), whose nature is still debated. Together, LBVs, LRNe and ILRTs make up a wider class of objects with luminosity intermediate between classical novae and standard SNe, called ‘gap transients’ (see Pastorello & Fraser 2019 and Cai et al. 2022 for a review). While their physical origin may be remarkably different, all these transients have one thing in common: the presence of optically thick CSM surrounding the system. The resulting similarity among the spectra of the gap transients and SNe IIn makes a proper classification of a newly discovered transient quite difficult: it can be challenging to unmask an impostor (Ransome et al. 2021).

Photometric follow-up can provide some important clues for this type of investigation. The light curve shape can be a useful indicator for classification: LBVs alternate periods of quiescence with erratic and powerful outbursts (Humphreys & Davidson 1994), LRNe often show distinctive double-peaked light curves, while ILRTs are characterised by SN-like light curves (Pastorello & Fraser 2019). It is still essential to complement the photometric follow-up with a spectroscopic study to characterise each class, despite the partial degeneracy in the properties of these transients. From a spectroscopic point of view, ILRTs can be summarily described as a black-body continuum with narrow emission lines superimposed. Strong Balmer emission lines dominate their spectra, together with several Ca features: Ca II H&K in absorption, strong Ca II NIR triplet in emission, and the [Ca II] forbidden doublet. As opposed to LRNe, ILRTs show no sign of molecular bands in the late phases of their evolution (Pastorello et al. 2019). A key difference between ILRTs and SNe IIn is that both the peak observed temperature ($T_{\text{ILRT}} \sim 7500$ K) and peak luminosity ($L_{\text{ILRT}} \lesssim 5 \times 10^4 L_{\odot}$) of ILRTs are significantly lower compared to SNe IIn, which instead tend to be hot ($T_{\text{IIn}} \sim 10\,000$ K, Taddia et al. 2013, but up to $\sim 15\,000$ K, e.g. Reguitti et al. 2022) and even brighter than average SNe II (e.g. Kiewe et al. 2012). The photospheric temperature and luminosity observed for SNe IIn can be sustained for as long as years (e.g. Tartaglia et al. 2020), thanks to the interaction between fast ejecta and slow-moving CSM, a mechanism that can efficiently convert kinetic energy into radiation (Smith 2017). When the interaction region between ejecta and CSM is visible, specific spectral features can be identified, most notably a blue shoulder on the $H\alpha$ line (Taddia et al. 2020). ILRTs, however, do not show clear signs of strong dynamical interaction between ejecta and CSM in their spectra: their low temperature and luminosity could imply a rather weak ejecta–CSM interaction, or at least that this interaction is hidden underneath layers of unshocked CSM.

As mentioned above, the physical mechanism behind ILRTs is still debated. As the photosphere lies within an optically thick gas shell, it is not possible to probe the material underneath the CSM, which could reveal key information on the nature of the transient itself. This uncertainty has led to a variety of interpretations regarding their true nature. Some researchers have advocated outbursts of post-main sequence stars (Kashi et al. 2010; Humphreys et al. 2011), while others have suggested that ILRTs are the result of jets originating from interacting binary stars (Soker & Kaplan 2021). Finally, ILRTs were also associated with electron capture supernovae (ECSNe; e.g. Nomoto 1984; Kitaura et al. 2006) originating from super asymptotic giant branch (AGB) stars (Botticella et al. 2009; Pumo et al. 2009; Cai et al. 2021). ECSNe are expected

to have some distinctive features that separate them from classic Fe core-collapse events. As was discussed for SN 2018zd, nebular spectra of ECSNe are expected to show Ni features stronger than Fe lines due to the different nucleosynthesis yields in the two scenarios (Hiramatsu et al. 2021; Callis et al. 2021). Indeed, Jerkstrand et al. (2017) provide synthetic nebular spectra of a $9 M_{\odot}$ Fe core-collapse SN and approximate the behaviour of an ECSN by enhancing the Ni content in their Fe core-collapse model. The Ni-enriched spectra display particularly strong [Ni II] emission lines. Until now, such an analysis has not been performed for ILRTs due to the lack of high-quality nebular spectra, as well as the lack of detected features beside the ones originating in the CSM.

In this paper, we present and analyse the spectra of four ILRTs following the photometric analysis of the same targets performed in ‘A study in scarlet I. Photometric properties of a sample of intermediate-luminosity red transients’ (Valerin et al. 2025; hereafter ‘Paper I’). The work is structured in the following manner: in Section 2, we describe the data reduction techniques. In Section 3, we present the optical and NIR data collected. In Section 4, the line luminosity and velocity are measured and compared within the sample. Section 5 presents our study of the high-resolution spectroscopy obtained for NGC 300 2008OT-1, while in Section 6, we discuss the broad features appearing in the late time spectra of NGC 300 2008OT-1 and AT 2019ahd. Finally, in Section 7, we summarise our work and draw conclusions.

2. Data reduction

The analysis presented in the following sections is based on the spectroscopic observations of four different ILRTs over the course of several months. Our follow-up campaigns are focused on the optical and NIR domains, employing several telescopes equipped with different instruments. The data reduction procedure is based on the Image Reduction and Analysis Facility (IRAF, Tody 1986, 1993), software specifically designed for image processing developed within the astronomical community. Every image undergoes the same preliminary reduction procedure: trimming, and bias and flat-field correction. NIR spectra undergo an additional sky subtraction step when combining the different nodding positions. A 1D spectrum of the target is extracted from the 2D image while a background subtraction is simultaneously performed in order to avoid contamination from the sky emission lines and the host galaxy signal. The 1D spectrum is then calibrated in wavelength on standard spectral lamps, typically showing He, Ne, Ar, Hg, and Kr lines. These procedures are repeated on the spectrum of a standard star (belonging to the list of European Southern Observatory spectrophotometric standards¹), which is routinely obtained during every observation run. Thanks to the comparison between the observed and tabulated flux values of a standard star, it is possible to accurately flux calibrate the spectrum of the target. Standard star observations are also useful to remove the telluric absorption features that affect ground-based observations. An additional, wavelength-independent flux calibration is performed, ensuring that the spectrum flux matches the values obtained from coeval photometric observations. Finally, each spectrum is corrected for redshift and reddening, in particular assuming a reddening law of $R_V = 3.1$ both for Galactic and internal extinction (Cardelli et al. 1989). The distance, reddening and redshift adopted for each

¹ <https://www.eso.org/sci/observing/tools/standards/spectra/stanlis.html>

Table 1. Key information regarding the transients in the sample.

Transient	Host Galaxy	Redshift	Distance [Mpc]	A_V [mag]
AT 2019abn	M51	$1.54 (-) \times 10^{-3}$	8.6 (0.1)	1.94 (0.20)
AT 2019ahd	NGC 3423	$3.35 (0.01) \times 10^{-3}$	11.1 (0.7)	0.39 (0.06)
AT 2019udc	NGC 718	$5.78 (0.03) \times 10^{-3}$	19.9 (1.4)	0.104 (0.001)
NGC 300 OT	NGC 300	$4.91 (0.01) \times 10^{-4}$	1.92 (0.14)	0.97 (0.15)

transient are summarised in Table 1; see Paper I for a discussion on the choice of the values used.

Many facilities and instruments were involved in the follow-up campaigns of our targets. The backbone of our spectroscopic monitoring was obtained within the ‘NOT Unbiased Transient Survey 2’ collaboration (NUTS2, Holmbo et al. 2019) through the Nordic Optical Telescope (NOT) equipped with the ‘Alhambra Faint Object Spectrograph and Camera’ (ALFOSC) and the ‘Nordic Optical Telescope near-infrared Camera’ (NOTCam), with crucial support from the instruments available within the ‘Global Supernova Project’ (GSP, Howell 2019). Other telescopes used during this project include the Gran Telescopio Canaria (GTC) equipped with the ‘Optical System for Imaging and low-intermediate-Resolution Integrated Spectroscopy’ (OSIRIS), the *William Herschel* Telescope (WHT) equipped with the ‘auxiliary-port camera’ (ACAM) and ‘Long-slit Intermediate Resolution Infrared Spectrograph’ (LIRIS), the South African Large Telescope (SALT) equipped with the ‘Robert Stobie Spectrograph’ (RSS), and the New Technology Telescope (NTT) plus ‘ESO Faint Object Spectrograph and Camera 2’ (EFOSC2), thanks to the advanced ‘extended Public ESO Spectroscopic Survey for Transient Objects Survey’ consortium (ePESSTO+, Smartt et al. 2015). Additionally, multiple spectra of NGC 300 OT were taken with the 6.5 m *Magellan* Telescopes, and the 4.0 m R-C Spectrograph at the Cerro Tololo Inter-American Observatory, and with the Very Large Telescope (VLT), most notably a high-resolution spectrum with the ‘Ultraviolet and Visual Echelle Spectrograph’ (UVES, Dekker et al. 2000) and a late spectrum with *X-Shooter* (Vernet et al. 2011). We also integrated our dataset with some publicly available spectra to have a more complete sampling of each event (Jha et al. 2019 for AT 2019ahd and Karambelkar et al. 2023 for AT 2019abn). The detailed logs listing all the spectroscopic observations for each target are reported in Tables A.1, A.2, A.3 and A.4.

3. Overview of the data

3.1. Optical spectra

Spectral sequences obtained for NGC 300 OT, AT 2019abn, 2019ahd and 2019udc are displayed in Figures A.1, A.2, A.3, A.4, A.5, and A.6. All spectra were corrected for redshift and total extinction along the line of sight: the values adopted for these corrections are reported in Table 1. The most prominent features noticeable in these objects are the emission lines of the Balmer series. Their narrow profiles ($\lesssim 1000 \text{ km s}^{-1}$) indicate that the spectral lines are forming in a region where the material is moving slowly, compatible with an opaque CSM. We do not detect clear *P*-Cyggni profiles in the emission lines, which would be caused by absorbing gas approaching the observer along the line of sight. The absence of the *P*-Cyggni features may imply that the photosphere of the transient is located at the

outer edge of the CSM, that the transient is intrinsically asymmetric, or that the covering fraction of the absorbing material is low. The Ca II H & K absorption lines ($\lambda\lambda 3934, 3968$) are found in all objects, especially at early phases. The photons absorbed through the Ca II H & K resonance lines excite the electrons of the Ca II atoms from the ground state $3s^2 3p^6 4s^2 S_{1/2}$ to $3s^2 3p^6 4p^2 P^o_{1/2, 3/2}$. From this energy level the electrons can radiatively decay to the level $3s^2 3p^6 3d^2 D_{3/2, 5/2}$, giving rise to a triplet of lines ($\lambda\lambda 18498, 8542, 8662$). Indeed this Ca II NIR triplet is detectable at most epochs in ILRTs, and becomes dominant at later times, as displayed in Figures A.2 and A.4. The compatible shape of the Ca II NIR and Ca II H&K lines in velocity space corroborates this interpretation (e.g. see Figure 7).

Finally, the transition that closes this ‘loop’ entails the de-excitation of the electrons from the level $3s^2 3p^6 3d^2 D_{3/2, 5/2}$ back to the ground state $3s^2 3p^6 4s^2 S_{1/2}$. This transition, which produces the [Ca II] doublet ($\lambda\lambda 7291, 7323$), is forbidden. Even if the metastable energy level $3s^2 3p^6 3d^2 D_{3/2, 5/2}$ is populated, the formation of [Ca II] requires a large amount of gas at moderate excitation and most of all at low density (e.g. Merrill 1958). Moreover, in a dense environment, collisions with other atoms or ions de-excite the electrons back to the ground state before the radiative decay process can take place, consequently suppressing the formation of these lines (e.g. Humphreys et al. 2011). Therefore, this spectral feature is only found in regions where the gas density is below the critical density $N_{\text{crit}} \sim 10^7 \text{ cm}^{-3}$ (for temperatures typically found in ILRTs, adopting the collision strength reported by Meléndez et al. 2007). Based on these premises, the ubiquitous presence of the [Ca II] doublet is one of the most characteristic features in ILRT spectra. While not unique to ILRTs, the persistent presence of the [Ca II] forbidden doublet in all the objects analysed so far has been proposed as a key feature to distinguish ILRTs from other transients that present similar spectra (Pastorello & Fraser 2019).

Another noteworthy feature in the low-resolution optical spectra of our sample of ILRTs is the presence of O I lines. In the spectra of all the considered objects the O I triplet $\lambda\lambda 7771.9, 7774.2, 7775.4$ is found in absorption. This triplet is detected at multiple epochs in NGC 300 OT (Figure A.1), AT 2019abn (Figures A.3 and A.4) and AT 2019ahd (Figure A.5), while in the case of AT 2019udc it is confidently detected only in the GTC spectrum obtained on 2019 November 22, 8 days after maximum. The O I triplet in absorption is a sign that the metastable level $2s^2 2p^3 (^4S^o) 3s^5 S^o_2$ is populated. We do not detect any emission lines from transitions that may feed this energy level: first of all, the $\lambda\lambda 7771.9, 7774.2, 7775.4$ triplet is never clearly detected in emission at any epoch, but we also do not detect transitions from higher energy levels (e.g. O I $\lambda 3947$). This suggests that the electrons populated the metastable energy level $s^2 2p^3 (^4S^o) 3s^5 S^o_2$ by recombination after an initial excitation. With time, the O I absorption triplet becomes less pronounced, until its detection becomes uncertain in the latest phases. The

absence of a clear emission component of the O I triplet could be due to efficient absorption by electrons in the metastable energy level. A few months after maximum luminosity, there is also the appearance of the O I $\lambda 8446$ emission line, which becomes progressively more prominent with time. This feature appears around +155 d in AT 2019abn, around +93 d in AT 2019ahd, and at around +123 d in NGC 300 OT (but this emission line is detected already in the high-S/N spectrum at +47 d as discussed in Section 5). This feature is not found in the spectra of AT 2019udc, but its spectroscopic monitoring had to be stopped at +67 d, and therefore this emission line could have developed after the end of our observational campaign. The appearance of the O I $\lambda 8446$ line is particularly interesting, as it cannot be the result of the de-excitation of O I atoms, which would result in the coeval formation of the $\lambda\lambda 7771.9, 7774.2, 7775.4$ triplet in emission. As discussed above, the O I triplet has been clearly detected in absorption, while its presence in emission is uncertain. For this reason, we favour a scenario in which the O I $\lambda 8446$ emission line found in ILRTs is the consequence of UV pumping, in agreement with the interpretation provided by Humphreys et al. (2011) and Moran et al. (2024). This process is also known as Bowen fluorescence, and is caused by the resonance between the Ly β $\lambda 1025.72$ Å and the O I $\lambda 1025.76$ line, which excites the electrons from the ground level $2p^4\ ^3P_2$ to $2p^33d\ ^3D_3^0$ (Osterbrock & Ferland 2006). The electrons subsequently decay to the levels $2p^33p\ ^3P_2$ (emitting $\lambda 11287$ Å), and $3p^33s\ ^3S_1^0$ (emitting $\lambda 8446$ Å) and finally back to the ground state (through the UV triplet $\lambda\lambda 11302.2, 1304.9, 1306.0$). Indeed, in the NIR spectra of NGC 300 OT presented in the following section, we detect the O I $\lambda 11287$ Å emission line, corroborating the fact that in these ILRTs we are observing the fluorescence process described above, rather than a different pumping mechanism (e.g. see the different processes described by Shore & Wahlgren 2010). As the excitation of the O I electrons to the $2p^33d\ ^3D_3^0$ energy level requires Ly β photons, the appearance of prominent O I $\lambda 8446$ Å at relatively late phases (and not at early ones) needs to be addressed. In the context of faster ejecta expanding underneath a slow-moving CSM, the Ly β could be shifted off resonance due to Doppler effect: more precisely, to have a perfect wavelength match, the Ly β photons should be redshifted by 11.7 km s^{-1} with respect to the oxygen atoms. In the early phases, when the resonant lines are opaque, the Ly β escapes the ejecta from a compact pseudophotosphere that is moving faster than the CSM above, greatly reducing the coupling between the Ly β and the O I $\lambda 1025.76$ line. As time progresses and the ejecta expand, the opacity of the lines drops and the redshifted Ly β photons that can trigger the Bowen fluorescence finally reach the CSM, which explains the delayed appearance of the O I $\lambda 8446$ line.

It is worth noting that all spectra of ILRTs in our sample become bluer during the rise to maximum: such behaviour is observed in other interacting transients (e.g. SN 2023ixf, Hiramatsu et al. 2023) and predicted by models of interacting SNe (Dessart et al. 2016), and therefore it could be a result of increasing interaction between the ejected material and the CSM. This interpretation is also supported by the increasing flux of the emission lines during the rise to maximum luminosity in all observed ILRTs (see Section 4.1). Finally, the late time spectra (≥ 100 days) collected for NGC 300 OT, AT 2019abn and AT 2019ahd do not show clear blueshift, nor do they change in terms of the shape of the emission lines. These are telltale signs of dust along the line of sight, and dust formation was inferred for these objects in Paper I from the NIR excess in their spec-

tral energy distribution (SED). A possible explanation for the lack of these spectroscopic signatures may be that the dust is not located along the line of sight: in this scenario, ILRTs would be intrinsically asymmetric events. Figure 1 displays spectra of six ILRTs taken in the first weeks after maximum luminosity. In addition to the four targets in our sample, we also show SN 2008S (Botticella et al. 2009) and AT 2017be (Cai et al. 2018). The former is considered a prototype of the ILRT class thanks to its prominent Ca lines, with a peak luminosity well in line with our sample of objects, while the latter, on the other hand, lies at the lower end of the luminosity distribution of ILRTs (see Figure 5 of Paper I). The right panels of Figure 1 show a zoom onto the most defining features of this class, in particular the [Ca II], Ca H&K, and H α lines. The strength of each feature varies among the sample: for instance, AT 2019udc is characterised by a strong Ca H&K absorption, while the [Ca II] doublet is most prominent in NGC 300 OT and SN 2008S. Albeit present, the Ca II NIR triplet becomes more prominent in all ILRTs at later phases.

3.2. Near-infrared spectra

In addition to the optical spectra, we gathered a total of five NIR spectra of our targets. NIR spectra of AT 2019abn were collected during the early rise, immediately after discovery. The single spectrum available for AT 2019udc was taken in a more advanced phase, three weeks after peak luminosity. Finally, the two spectra of NGC 300 OT monitor the object at late phases, hundreds of days after maximum light. As displayed in Figure 2, AT 2019abn and AT 2019udc appear to be quite similar: a nearly featureless continuum, without strong emission or absorption lines superimposed. Conversely, in the spectra collected for NGC 300 OT, it is possible to identify several emission features. Most notably, these include hydrogen lines of the Paschen (Pa $\beta, \gamma, \delta, \epsilon$) and Brackett series (Br γ), and He I ($\lambda 10830$), O I ($\lambda 11287$), and Fe I ($\lambda\lambda 15831, 16679, 16693$). As mentioned in the previous section, the detection of O I $\lambda 11287$ Å has been key in confirming that the optical line O I $\lambda 8446$ Å is produced by the Bowen fluorescence.

4. Line parameters

4.1. Line luminosity

In this section we estimate the parameters of the main lines observed in our spectra. In order to avoid an additional source of systematic uncertainty, we do not assume a specific line profile (e.g. Gaussian or Lorentzian). Instead, we estimate the luminosity contribution of a given feature by integrating the flux over the continuum in the considered spectral region. This procedure is repeated multiple times in order to estimate the error associated with the measurement. The measured line flux is then converted into the luminosity of the line by accounting for the distance of the transient (the spectra were already corrected for extinction during the calibration procedure). The luminosity evolution of H α , H β , the Ca II NIR triplet, and the [Ca II] doublet is shown in Figure 3. In each panel we also represent the continuum level in the proximity of each spectral feature as a solid line. For clarity, the continuum level is scaled to match the line luminosity at the first measured epoch. The continuum was estimated in the range 4725–4825 Å for H β , 6700–6850 Å for H α and [Ca II], and 8200–8350 Å for the Ca II NIR triplet. In the same figure, the bottom panels report the equivalent widths (EW) for Na ID and Ca II H&K in absorption. We note that the spectral features

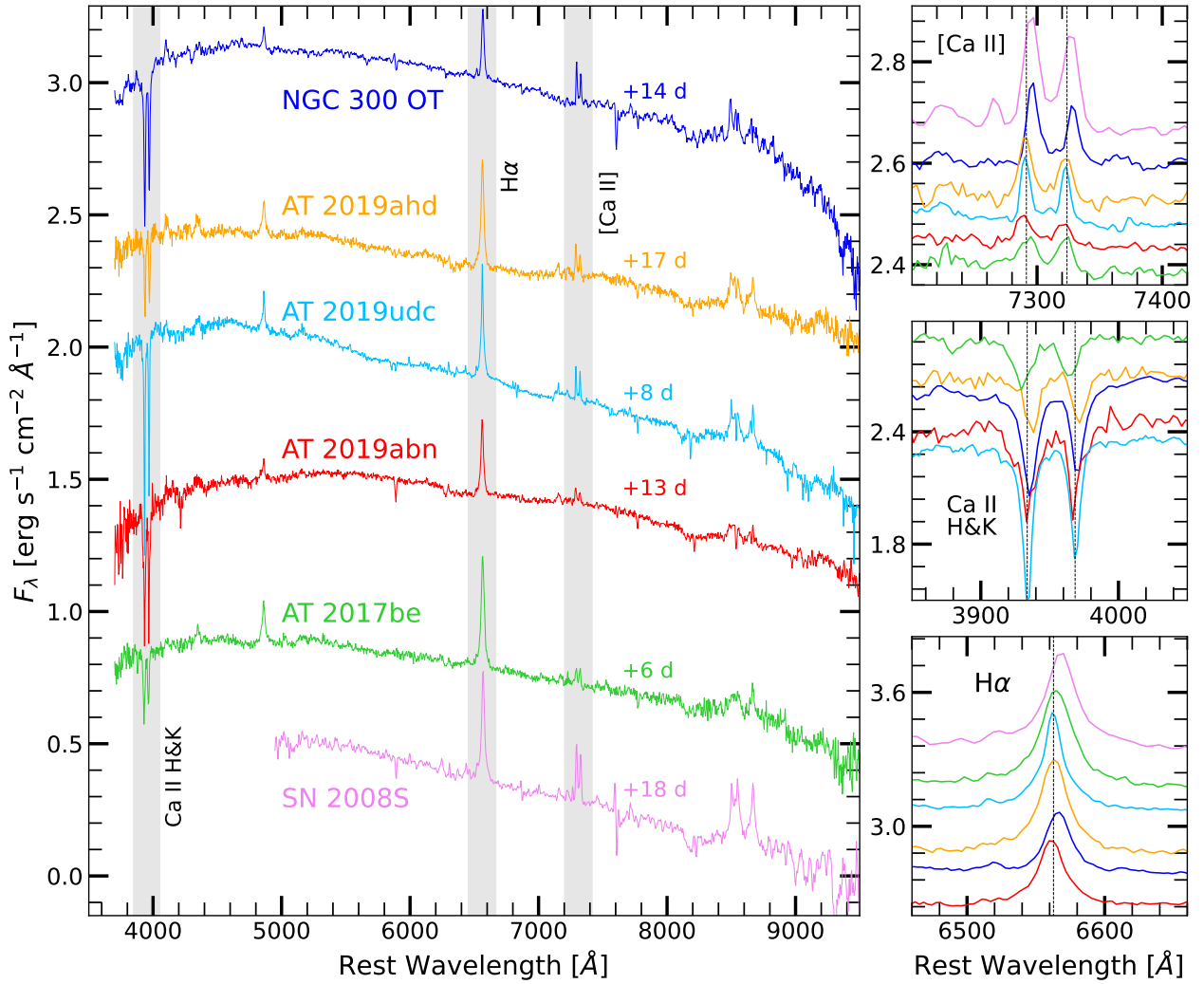


Fig. 1. Comparison between early spectra of our sample of ILRTs, taken in the first weeks after peak luminosity (phases are reported with respect to maximum light). The right panels show a more detailed view of the [Ca II], Ca II H&K and H α lines.

examined can present multiple components in high resolution (see in particular Section 5), and therefore the values reported here track the behaviour of the sum of all components of each line. An additional complication is given by the fact that in the case of optically thick lines we are not sampling the whole emitting volume.

Considering the emission features, we note that the luminosity evolution of H α and Ca II NIR triplet is not monotonic: after an early peak, the luminosity declines sharply over the course of a few weeks. A minimum is then reached, and subsequently the lines start to strengthen again, forming a sort of broad, long-lasting second peak. This trend is even more clear when compared to the evolution of the spectral continuum at the same phases, which monotonically declines after maximum brightness. The same evolution can be detected in H β , albeit less pronounced. For NGC 300 OT, only the second broad peak is visible, because the object was behind the Sun during the first phases of its evolution. This line re-brightening has already been noted in other ILRTs and was tentatively attributed to CSM interaction (Cai et al. 2018). In this scenario, there is a collision between rapidly expanding ejecta and the slower CSM lying above. The energy released from this interaction could lead to the re-ionisation of the gas above, and its subsequent recombination. The fact that the re-brightening of the hydrogen

emission lines is coeval with the Ca II NIR strengthening (see Figure A.7) suggests that these features originate in a similar environment and are produced by material undergoing similar physical processes. At the same time, we note that during this re-brightening of the lines there are no relevant changes in the ionisation state nor in the profile of the lines in the low-resolution spectra, which are typical telltale signs of ongoing interaction. This means that either the CSM along the line of sight is optically thick enough to hide the interaction region, or that the secondary peak in line luminosity is caused by a mechanism other than CSM interaction. An alternative scenario to CSM interaction could be the presence of material that is reached by the photons produced by the transient only after some time after its onset. This material would become excited through interaction with photons, producing Balmer and Ca II NIR emission lines as it becomes de-excited. By assuming spherical symmetry and considering the light-travel time, the location of the inner radius of the emitting CSM can be estimated thanks to the epoch at which the emission lines reach their maximum luminosity, through $R \approx t_{\max}c/2$ (see the geometry described in Figure 6 by Miller et al. 2010). In principle, this reasoning can be applied to both the first and second luminosity peak observed in the emission lines of ILRTs. In this scenario, the first luminosity peak would be caused by CSM with an inner radius of $\approx 1.3 \times 10^{16}$ cm

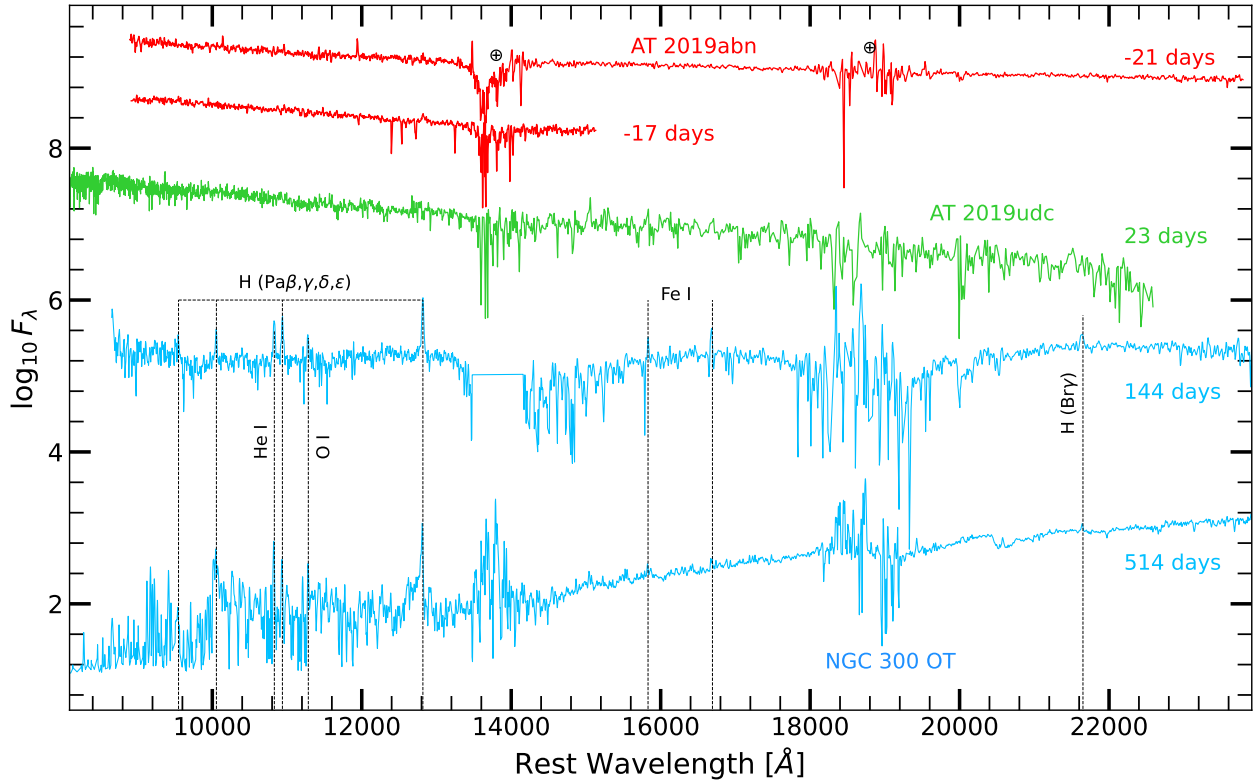


Fig. 2. Sequence of NIR spectra collected for our sample of ILRTs. AT 2019abn is shown in red, AT 2019udc in green and NGC 300 OT in blue. The most prominent emission lines are marked on the spectra of NGC 300 OT. The positions of telluric features are marked with a circled plus symbol. The first spectrum of AT 2019abn displayed is the combination of two spectra obtained at phases -21 and -20 days with respect to maximum.

for AT 2019ahd and AT 2019udc ($t_{\max} \approx 10$ days), while the luminosity peak of AT 2019abn would lead to the inference of an inner CSM radius of $\approx 2.7 \times 10^{16}$ cm ($t_{\max} \approx 21$ days). Given that the secondary luminosity maximum occurs at remarkably later phases (≈ 90 days for NGC 300 OT, up to ≈ 150 days for AT 2019abn), the CSM responsible for this emission would be located at $\approx 1.2 \times 10^{17}$ cm for NGC 300 OT, and up to $\approx 2 \times 10^{17}$ cm for AT 2019abn. In any case, the secondary luminosity peak observed for the emission lines favours the scenario of a complex environment surrounding ILRTs, which could have been formed by a stellar wind or eruptive episodes of the progenitor star.

Whatever the mechanism driving its evolution, the marked rebrightening shown by the Ca II NIR and H α lines is a characteristic commonly found in ILRTs. In contrast, the luminosity of the [Ca II] forbidden doublet displays an overall monotonic decline. We point out that the [Ca II] evolution appears to mimic the shape of the continuum luminosity in all four objects. This behaviour is consistent with the fact that the [Ca II] doublet originates from low-density gas, farther from the dense CSM. Its evolution is therefore dictated by the incoming radiation from the transient, in particular by the radiation absorbed by the Ca H&K lines. As previously described, there can only be emission of the [Ca II] doublet if the medium is below the critical density. In this configuration, the hypothetical interaction between ejecta and CSM can cause the collisional excitation of Ca and H atoms in the dense CSM, which is above the critical density for the production of the [Ca II] doublet, therefore resulting in a rebrightening only for Balmer and Ca II NIR triplet lines. At the same time, the slow material producing [Ca II] lines is too distant to be affected by the collision and keeps following the evolution of the spectral continuum.

The Na ID EW depends on the properties of the CSM, the interstellar gas along the line of sight, possible ejecta and even the viewing angle in the case of non-spherically symmetric ejecta. For these reasons, its behaviour is seen to vary significantly within the sample. AT 2019udc shows a strong Na ID feature in the first two observed epochs (EW ~ 5 Å), which become rapidly weaker during the following days: a similar behaviour was observed for the ILRTs AT 2010dn and AT 2012jc (Cai et al. 2021; Byrne et al. 2023). On the contrary, AT 2019abn initially displays a weak Na ID absorption feature (EW ~ 1 Å), which becomes more significant in the following weeks (up to EW ~ 3 Å). AT 2019ahd and NGC 300 OT present similar behaviour, although scaled down compared to AT 2019abn. The increase and following decrease in the EW of the Na ID over time can be qualitatively reproduced by considering the column density of Na I laying in front of a shock travelling through a thick CSM (Byrne et al. 2023): in this simple scenario, the recombination of Na II is responsible for the initial increase in the Na ID EW, while the shock travelling outward and sweeping the gas eventually causes its decline. Finally, the EW evolution of Ca II H&K appears to be quite similar in AT 2019ahd and AT 2019udc: an initial rapid decline followed by a somewhat broad ‘peak’. NGC 300 OT, missing the first phases of evolution, displays a slow decline in EW, which resembles the evolution of AT 2019udc in particular. In stark contrast with the behaviour of the other three ILRTs, AT 2019abn displays Ca II H&K absorption features that become significantly more pronounced after the first month of evolution. In principle, high-resolution and multi-epoch observations of Na ID and Ca II H&K components in ILRTs would allow us to distinguish whether the evolution of these

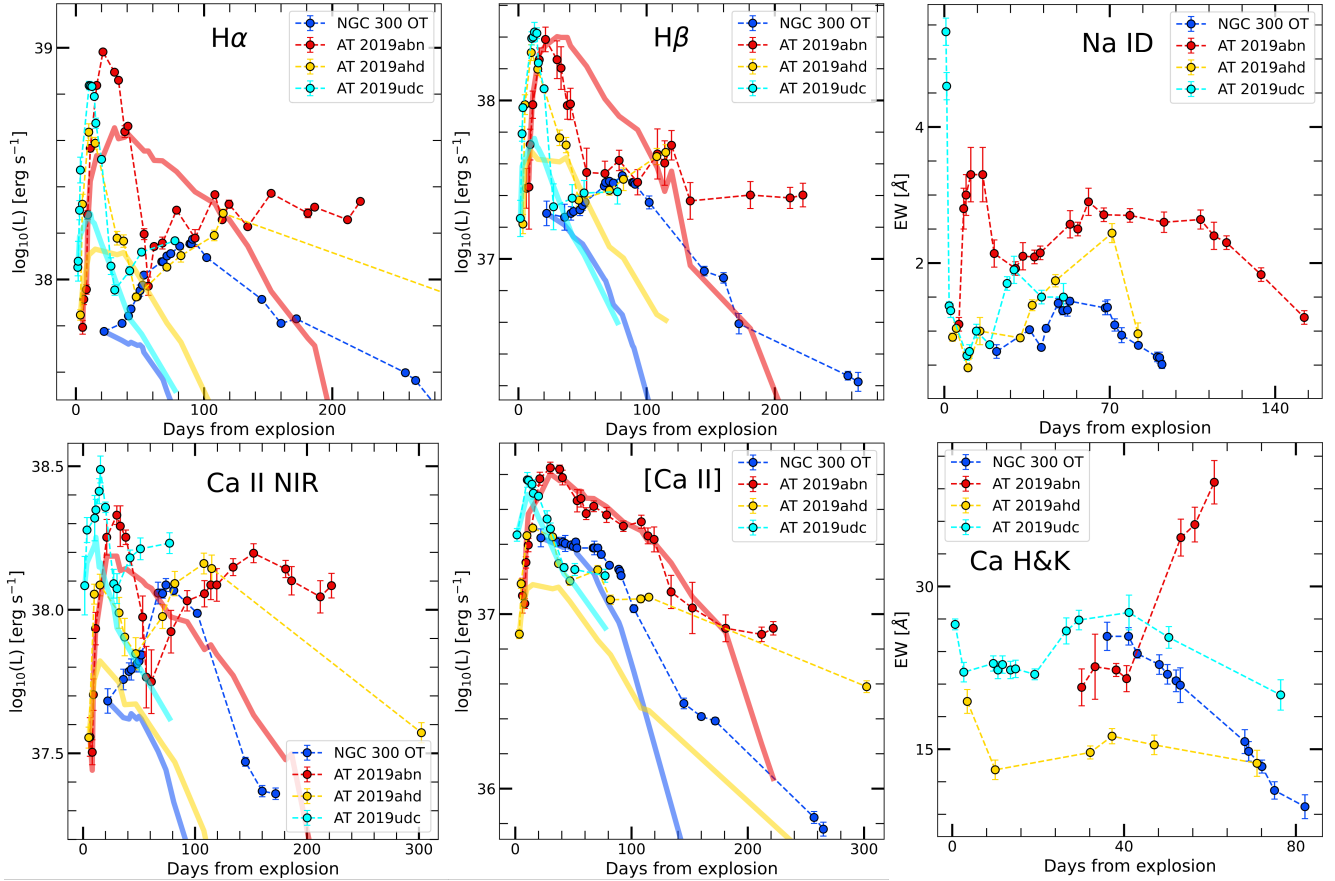


Fig. 3. Temporal evolution of the main spectral features for our sample of ILRT. The first two panels of each row show the luminosity of $H\alpha$, $H\beta$, the Ca II NIR triplet and [Ca II] with coloured circles. Solid lines represent the scaled level of continuum in the proximity of each feature. The last panels of each row show the EW of the Na ID and Ca II H&K absorption features.

absorption features is driven by a change in the ionisation state of the CSM or by the presence of clumps of matter, as prescribed by Patat et al. (2007). However, Na ID and Ca II H&K absorption features often saturate in ILRTs, even despite the broadening introduced by the velocity field: this inevitably hinders the physical interpretation of these measurements.

AT 2019abn, the brightest and longest-lasting ILRT observed to date, also displays the brightest $H\alpha$ and [Ca II] features among the sample, reaching $9.5 \times 10^{38} \text{ erg s}^{-1}$ and $6.9 \times 10^{37} \text{ erg s}^{-1}$ at peak luminosity, respectively. Conversely, NGC 300 OT is characterised by the least luminous Balmer lines within the sample. However, beside the simple luminosity of these emission features, it is useful to investigate their evolution relative to other lines. For this purpose, in Figure 4 we track the change in value of the Balmer decrement ($H\alpha/H\beta$) over time for our sample of ILRTs. In their first spectra, both AT 2019ahd and AT 2019udc display large values for the Balmer decrement (>4 and >6 , respectively), which quickly decrease down to 2.2 and 2.4 in the following two weeks. AT 2019abn and NGC 300 OT do not show this early decline, but this can be caused by the absence of very early spectra, especially for NGC 300 OT. With time, the Balmer decrement of the whole sample grows significantly, reaching values of 8 and 22 for AT 2019abn and NGC 300 OT, respectively. The evolution of the Balmer decrement described above matches that observed in SN 2008S. Based on the measured values of the Balmer decrement and temperature at early phases, Botticella et al. (2009) constrain the electron density in the CSM to be $10^{10} \text{ cm}^{-3} < N_e < 10^{12} \text{ cm}^{-3}$, according to

the work performed by Drake & Ulrich (1980). Such high electron densities have already been found in the context of SNe II_n: for example, SN 2006gy presented an electron density in the CSM of above $6 \times 10^{10} \text{ cm}^{-3}$ (Smith et al. 2010).

However, these considerations are based on the assumption of case B recombination, meaning that the gas is optically thick for lines of the Lyman series and optically thin for lines of the Balmer series. Under these conditions, it has been shown that the Balmer decrement is close to ~ 3 for a wide range of temperature and density values of astrophysical interest (Osterbrock & Ferland 2006). As reported in Figure 4, ILRTs display a ratio $H\alpha/H\beta$ that varies with time, reaching values well above the expected one of ~ 3 . There are several possible explanations for this departure from case B recombination, such as the collisional excitation of H atoms, which would boost the $H\alpha$ luminosity, and dust formation, which would extinguish the $H\beta$ more than the $H\alpha$ (Drake & Ulrich 1980). Another mechanism that can cause an increase in the Balmer decrement is the increased opacity of the lines of the Balmer series, as explained by Osterbrock & Ferland (2006) (Chapter 4.5).

4.2. Width of the spectral features

Measuring the full width at half maximum (FWHM) of the emission lines of ILRTs can be challenging: narrow features such as the [Ca II] doublet are typically unresolved in our spectra. As previously done for the line flux, we do not assume a specific fitting function, but we manually measure the FWHM of

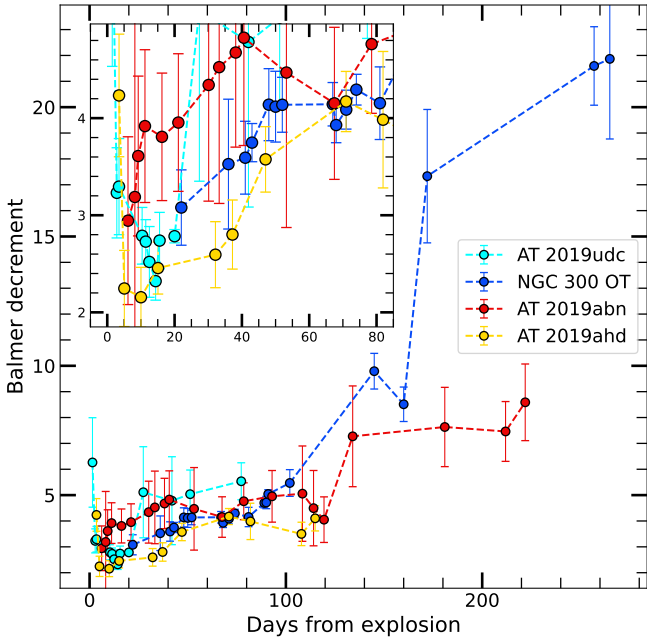


Fig. 4. Evolution of the Balmer decrement over time for our sample of ILRTs. A zoom onto the early phases is shown in the small panel.

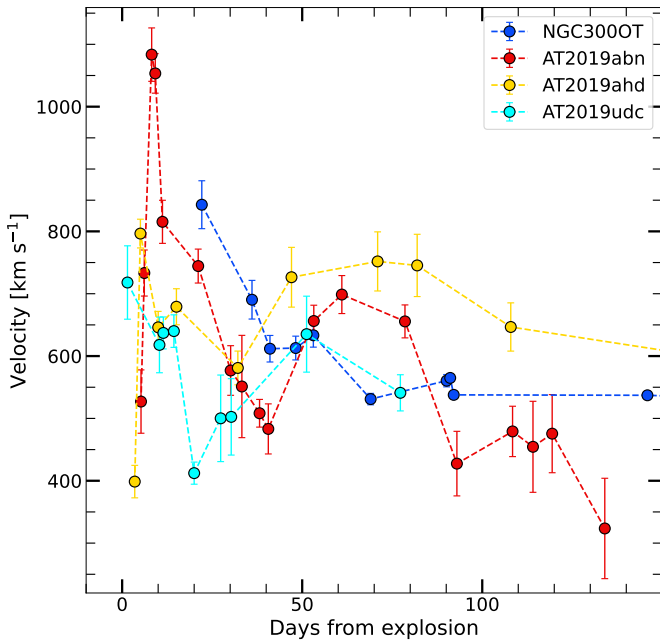


Fig. 5. FWHM velocity measured from the $H\alpha$ emission line in our sample of ILRTs during the first 150 days of their evolution.

the lines. The resulting FWHM is corrected for the resolution of the instrument (typical values of $R \sim 500$) and then converted into a FWHM velocity, which can be taken as an order of magnitude estimate of the speed at which gas is moving in the emitting region. This value, however, should not be treated as a precise velocity measurement: the broadening of the line profiles can be caused by the combination of a Doppler shift due to the bulk motion of the emitting material and by the electron scattering of the photons within a hot medium (Fransson et al. 2014). Electron scattering is more marked at higher electron temperatures and at higher optical depths, resulting in the appearance of extended wings (Huang & Chevalier 2018). In Figure 5 we

display the FWHM velocities inferred from the $H\alpha$ line for our sample of ILRTs in the first 150 days of evolution. Analysing the $H\alpha$ line comes with the significant advantage that this feature is bright at all epochs, therefore allowing an accurate FWHM measurement. Furthermore, especially at early times, the $H\alpha$ line is resolved in most spectra, and is not blended with other features (as happens for the Ca II NIR triplet), making it the ideal feature for comparing the evolution of different objects with our dataset.

During the earliest phases, when the luminosity is still rising, the FWHM velocity of $H\alpha$ quickly increases in AT 2019abn, AT 2019ahd, and AT 2019udc. AT 2019udc, on the other hand, displays the broadest FWHM in the first spectrum; it is impossible to confirm whether or not this is also the case for NGC 300 OT, as we are missing the pre-maximum part of its evolution. The ILRTs in our sample reach a peak FWHM velocity of between ~ 700 and 1100 km s^{-1} , with AT 2019abn as a clear outlier and the other three objects clustering around $v_{\text{FWHM}} \sim 800 \text{ km s}^{-1}$ at peak. After the maximum FWHM is reached, ILRTs display a rapid decline over the course of 3–5 weeks. Afterwards, NGC 300 OT settles at an almost constant $v_{\text{FWHM}} \sim 550 \text{ km s}^{-1}$ for over 100 days, while the other three transients are characterised by a secondary peak in v_{FWHM} after a local minimum, increasing by $\sim 200 \text{ km s}^{-1}$ in about 5 weeks. During this phase, AT 2019ahd displays the broadest lines, with a v_{FWHM} of up to 750 km s^{-1} . Eventually the $H\alpha$ narrows once again, down to 320 km s^{-1} at 135 days for AT 2019abn (and unresolved thereafter), 470 km s^{-1} at 302 days for AT 2019ahd and 170 km s^{-1} at 536 days for NGC 300 OT. The behaviour of the FWHM velocity described above shows remarkable differences from that of the photometric features of the transients. For example, NGC 300 OT is two magnitudes fainter than AT 2019abn (see Paper I), yet its FWHM velocity is not only compatible, but is oftentimes larger than that observed for AT 2019abn. It is important to stress that these FWHM velocities are linked to the properties of the CSM where the line is produced: as the line-formation region moves within the CSM, different values of gas speed, electron temperature and optical depth mould the profile of the lines, which is reflected in the evolution of the FWHM velocity shown in Figure 5. However, as in the case of SN IIn, the low FWHM velocities measured do not exclude the presence of fast ejecta lying below the CSM (e.g. Leonard et al. 2000).

5. High-resolution spectroscopy of NGC 300 OT

NGC 300 OT is the closest ILRT observed (see Cai et al. 2021 and Karambelkar et al. 2023 for a review of known ILRTs). Thanks to the proximity of its host galaxy ($1.92 \pm 0.14 \text{ Mpc}$), it was possible to obtain a high-resolution optical spectrum of the transient on 2008 July 02 with the VLT equipped with UVES, yielding a resolution between 0.12 and 0.36 \AA . Figure 6 shows the identification of the main spectral lines on this high-resolution spectrum. The measurements pertaining to the most prominent features are reported in Table 2, in particular their observed central wavelength, their FWHM, and their estimated flux. Apart from the H, Ca, O and Na lines discussed in the previous sections, which are also easily recognisable in the low-resolution spectra, with this high resolution and high S/N we find a number of metal lines, in particular Fe I ($\lambda\lambda\lambda 5535, 8688, 8757, 8824$), Fe II (multiplets 40, 42, 46, 49, 73, 74 and forbidden line $\lambda 7155$), Mg I ($\lambda 8806$), and Sc II lines (Moore multiplet 29). Additionally, we identify [O I] ($\lambda 6300, 6364$), the faint Ca II absorption doublet ($\lambda\lambda 8912, 8927$) and He I ($\lambda\lambda 5876, 6678, 7065$). All these features are narrow (FWHM $\lesssim 10 \text{ \AA}$) but resolved, and therefore originate within the

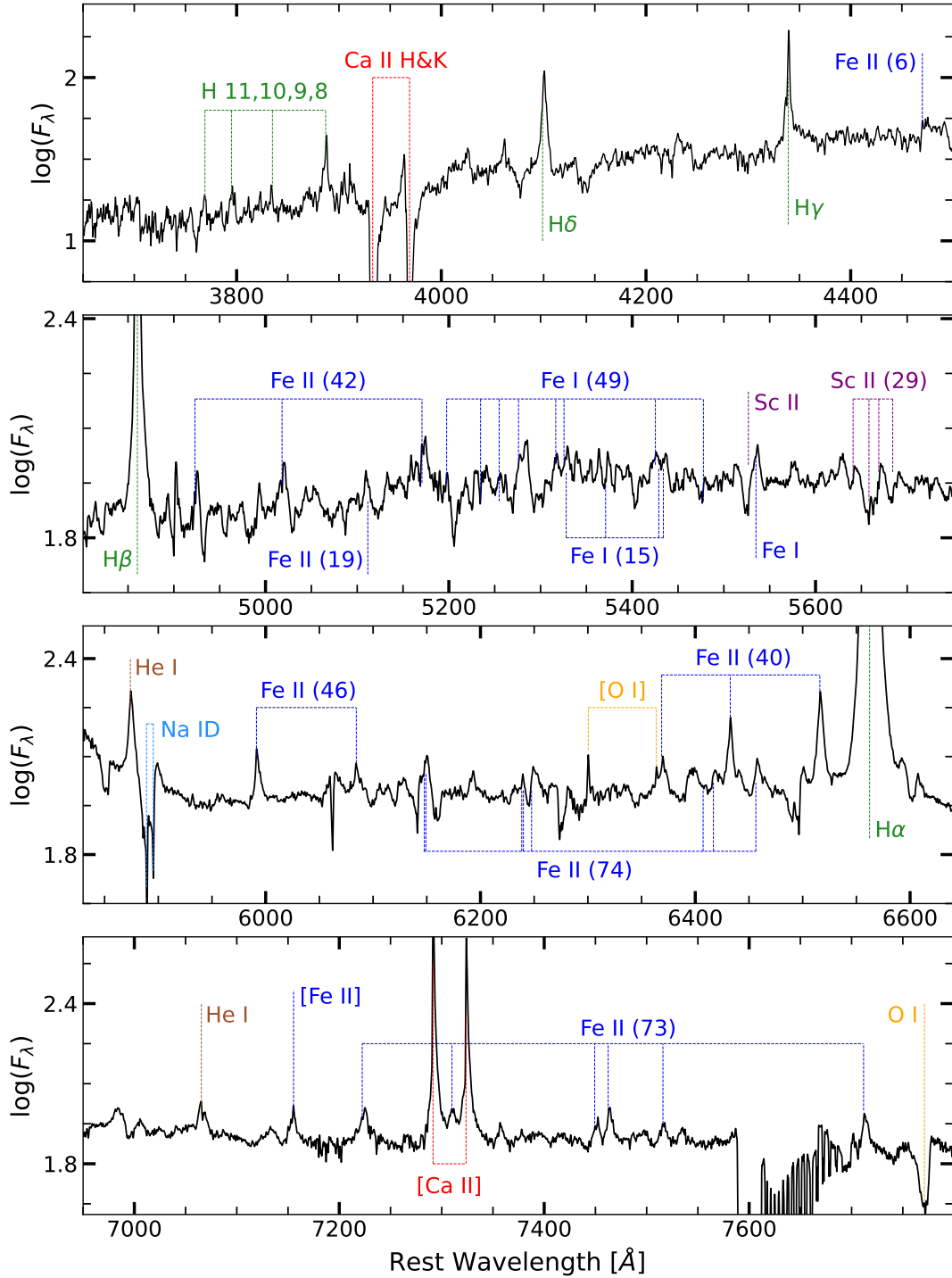


Fig. 6. Identification of the main spectral lines found in the UVES spectrum of NGC 300 OT taken on 2008 July 02. Lines originating from different elements are highlighted in different colours. The spectrum has been rebinned and scaled for clarity.

opaque CSM or above it. Thanks to the high-resolution spectrum, it is possible to accurately compare the FWHM velocities associated with different emission features. The broadest feature observed at this epoch is the $H\alpha$ emission line, with a FWHM velocity of 520 km s^{-1} . The Ca II NIR line $\lambda 8498$ is marginally narrower, with a FWHM velocity of 440 km s^{-1} : the fact that $H\alpha$ and Ca II NIR have compatible shapes in velocity space corroborates the scenario outlined in the previous section, where both these features are generated in neighbouring environments. The [Ca II] forbidden doublet is instead characterised by a FWHM

of 80 km s^{-1} , pinpointing its origin in a separated region likely characterised by lower gas velocity, electron temperature, and optical depth compared to the region where permitted lines are formed. The [O I] forbidden lines are comparable in FWHM and shape with the [Ca II] doublet. In general, the range of FWHM velocity displayed by the lines (Table 2) suggests a stratification in the emission lines of different ions, and even within the emission lines of the same ions.

Spectral features that appear simple in low resolution may actually hide a more complex structure, which can only be

Table 2. Main lines in the UVES spectrum of NGC 300 OT.

Line	λ_0 [Å]	λ_m [Å]	FWHM [Å]	Flux [10^{-15} erg s $^{-1}$ cm $^{-2}$]
H α	6562.8	6562.5	11.6	265.7
H β	4861.3	4860.3	5.8	64.3
H γ	4340.5	4339.4	2.4 ^(*)	20.7 ^(*)
H δ	4101.7	4100.7	5.0	16.7
Ca II NIR	8498.0	8495.9	12.6	105.3
[Ca II]	7291.5	7292.0	1.9	24.1
[Ca II]	7323.9	7323.4	2.0	17.3
Ca II H	3933.7	3933.9	6.4	–
Ca II K	3968.4	3968.9	4.7	–
Fe II (40)	6516.1	6516.7	6.0	11.7
Fe II (40)	6432.7	6432.8	4.9	7.6
Fe II (40)	6369.5	6368.7	6.2	5.2
Fe II (42)	5169.0	5170.7	7.0	7.7
Fe II (42)	5018.4	5018.6	8.0	6.4
Fe II (42)	4923.9	4925.2	5.2	3.4
Fe II (46)	5991.4	5992.5	4.5	4.8
Fe II (46)	6084.1	6084.4	6.2	3.8
He I	5875.6	5874.9	5.0	8.7
He I	7065.2	7065.7	8.2	4.2
[O I]	6300.3	6300.4	1.6	1.6
[O I]	6363.8	6363.9	1.6	0.7
O I	7771.9	7770.3	9.9	–
Na I	5889.9	5889.5	5.5	–
Na I	5895.9	5895.5	6.5	–

Notes. The columns report the identified line, its rest and measured wavelength, the FWHM and flux obtained as detailed in the text. Errors on the flux and FWHM measurements are of the order of 10%. The spectrum was redshift and reddening corrected with the values reported in Table 1. ^(*)Affected by absorption features, as described in Section 5.

unveiled through high-resolution observations. The shape of these lines carries relevant information on the geometry of the emitting region. In Figure 7 we show the profiles of the lines of the Balmer series, of some prominent Fe II lines, of the Ca features (NIR λ 8498, [Ca II] λ 7291 and Ca II K absorption), and of the Na ID absorption doublet. The H α line in the UVES spectrum shows a composite profile: superimposed to the emission line are two narrow absorption components. The most prominent absorption component has a FWHM of 30 km s $^{-1}$ and is only 15 km s $^{-1}$ redward of the rest wavelength of H α . The second absorption component is even narrower, with a FWHM close to the spectral resolution, and is situated 140 km s $^{-1}$ blueward of the emission peak. In the top left panel of Figure 7, the most prominent and redward of the two absorption features can be seen in other coeval lines of the Balmer series, although with lower S/N. The second, shallower and more blueward absorption does not have a counterpart in the other H lines, and therefore could result from a transition of a different element. The H γ line presents a unique shape that deviates from the trend of the other Balmer lines, showing in particular a marked absorption in the blue wing, which also results in a narrower FWHM. The same behaviour for the H γ line has been observed in the yellow supergiant IRC+10420, where it has been explained as the result of absorption components found in stellar atmosphere models (Figure 6 in Klochkova et al. 2002).

In the top right panel of Figure 7, it is possible to study the different profiles of the Fe II lines. Despite originating from the same atomic species, some lines display a dominant emission

component, with only traces of absorption at around the rest wavelength (e.g. λ 6517), while other lines display a more complicated profile, with marked absorption features and a redshifted emission component, compatible with a *P*-Cygni profile (e.g. λ 5018,5169). The Fe II lines that display a stronger absorption, such as the multiplet 42, are characterised by a larger oscillation strength, which favours self absorption. Additionally, the spatial stratification of the emission lines may further enhance this effect.

The analysis of the Ca II lines (bottom left panel of Figure 7) offers valuable insights into the geometry of the line-forming region. As mentioned, the Ca II NIR line λ 8498 displays a prominent absorption component with a FWHM of 30 km s $^{-1}$ situated just 10 km s $^{-1}$ blueward of the rest wavelength position of this line. On the other hand, the [Ca II] doublet presents a very different line profile: the line is markedly asymmetric, with the blue wing almost completely missing. Berger et al. (2009) tentatively attribute this behaviour to self absorption, in a scenario where the [Ca II] doublet originates in a low-density, inflowing gas. However, Humphreys et al. (2011) state that self absorption is quite rare for a forbidden transition such as [Ca II] (although not impossible, as shown for example by Mason & Shore 2022): the peculiar line profile is thought to be formed through electron scattering in an expanding envelope, which gives rise to the extended red wing observed. We expand on this interpretation, based on the similarity between the shape of the absorption feature superimposed to the Ca II (λ 8498) emission line and the [Ca II] doublet: a steep blue edge and an extended red wing (lower left panel of Figure 7). We deduce that both features are produced in the same region, in which the gas density must be low to allow the production of the [Ca II] doublet. The velocity field of the gas in this region shape both spectral features. We speculate that the observed asymmetry reflects the dynamics of a stellar wind that reached terminal velocity. By extension, all the observed narrow absorptions superimposed to the emission lines (Balmer lines, Ca II NIR triplet, He I, Fe II and O I) can be traced back to this pre-existing, low density wind produced by the progenitor star. With the redshift we adopted for NGC 300 OT, the blue cut-off for the [Ca II] is located at ~ -30 km s $^{-1}$, which provides an estimate of the terminal wind velocity in the scenario described above. This value is well in line with the wind velocities observed for AGB stars (e.g. Ventura et al. 2020). On the other hand, the red wing of the [Ca II] extends over 200 km s $^{-1}$ red-ward: this could be the result of photons scattered into the line of sight by interaction with free electrons. Indeed, a similar line profile has been obtained by simulating the scattering of an emission line within a stellar wind (Figure 10 in Huang & Chevalier 2018 and Figure 4 in Jerkstrand 2017).

In the Na ID absorption profile (bottom right of Figure 7), it is possible to differentiate multiple components: a narrow, barely resolved ($v_{\text{FWHM}} < 10$ km s $^{-1}$) component associated with the Milky Way gas (which is unchanging with time, according to Berger et al. 2009), a second narrow component associated with the host galaxy, NGC 300, and a broader absorption (FWHM velocity ~ 200 km s $^{-1}$ for each component of the doublet) originating from the gas expanding around the transient (for a more detailed discussion of Na ID in ILRTs, see Byrne et al. 2023). Lastly, the Ca II H line presents a FWHM velocity of 420 km, ruling out an interstellar origin in favour of production within the more turbulent CSM surrounding the transient. The other line of the doublet, Ca II K, is contaminated by the H ϵ emission line, resulting in a misleading asymmetric profile with a short blue wing and an extended red wing.

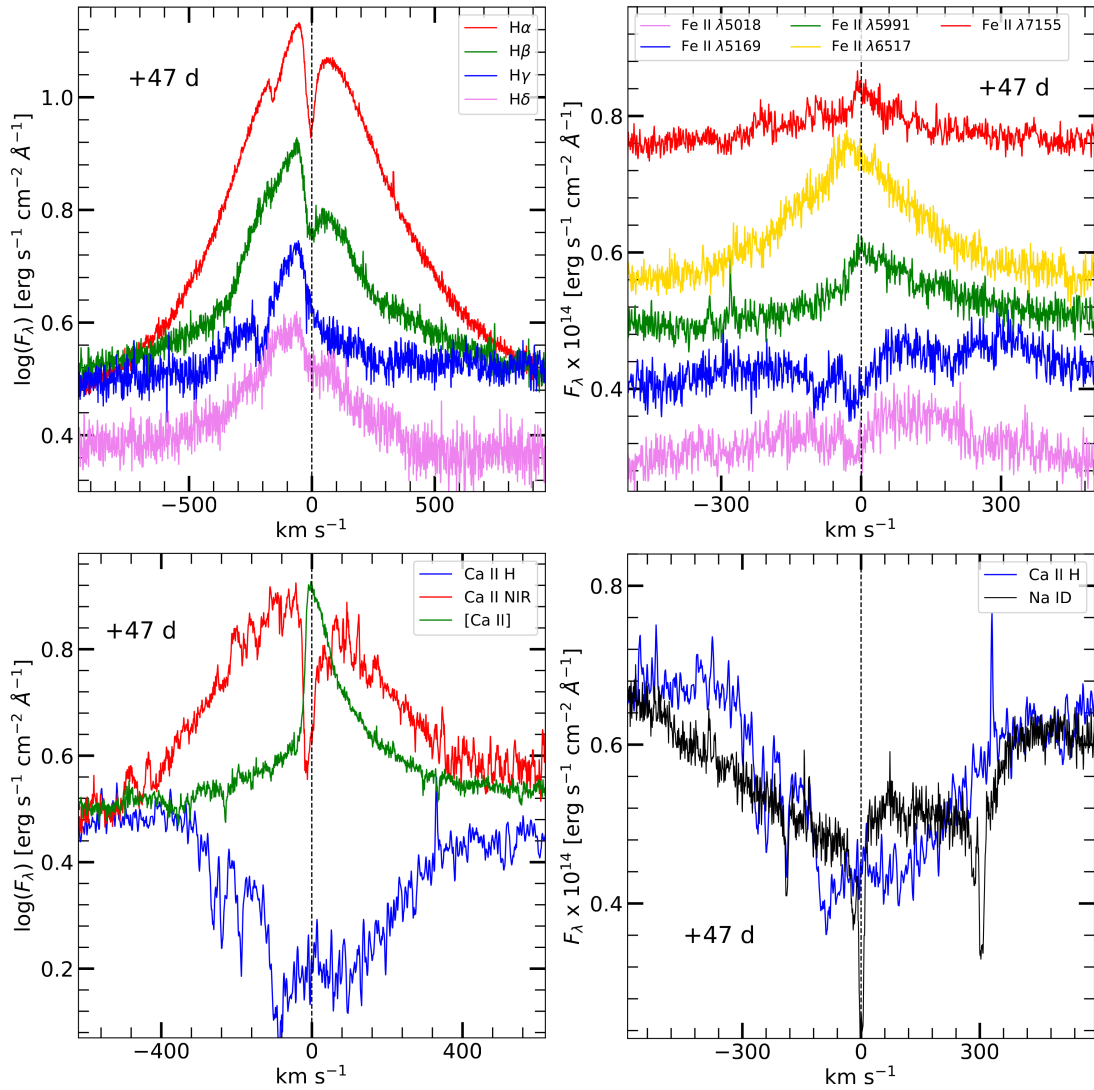


Fig. 7. Most prominent features in the high-resolution spectrum of NGC 300 OT displayed in velocity space. Top left panel: Lines of the Balmer series. Top right panel: Fe II lines. Bottom left panel: Ca II NIR, [Ca II] and Ca II H. Bottom right panel: Complex Na ID absorption features compared with the Ca II H absorption. Spectral features have been scaled in flux for clarity.

6. Broad features in late time spectra

Late-time spectra of ILRTs display some intriguing features. Both in NGC 300 OT and AT 2019ahd, two broad features start appearing at 6168 Å and 7002 Å, a few months after peak luminosity (the position of the peak was estimated through a Gaussian fit). Notably, no such broad lines have yet been detected in any spectrum of ILRTs. Figure 8 shows the late time spectra of NGC 300 OT and AT 2019ahd superimposed, in order to highlight the similarities between the two, in particular regarding these broad features. The red wing of the bluer feature (at 6168 Å) partially overlaps with the narrow [O I] λ 6300 line, while another emission feature can be detected at λ 6247. On the redder feature (at 7002 Å), there is minor contamination from He I λ 7065. It is challenging to exclude the presence of absorption components, similar to the ones detected in the H and Ca II NIR lines given the rather low S/N. Both broad features present a FWHM velocity of ~ 2500 km s⁻¹. The lower panels of Figure 8 show their evolution over time in NGC 300 OT, from their first detection at +123 d up to +243 d. Their development is remarkably slow, as the features appear barely different

after 120 days. Regarding AT 2019ahd, we only detect the broad emission components in a single spectrum, and therefore it is not possible to study their evolution over time. Given the rather symmetrical distribution of these broad features around the H α line, in principle they could be explained through H α emission from two fast jets of matter moving at $\sim 20\,000$ km s⁻¹ (based on the displacement of their peak with respect to the H α rest wavelength), one approaching and one receding along the line of sight. However, as the features appear to be almost identical in both AT 2019ahd and NGC 300 OT, it is extremely unlikely to have observed two jets orientated exactly in the same direction relative to the Earth, and therefore we disfavour this scenario.

In the context of a terminal, explosive event, it is tempting to associate these features with the products of nucleosynthesis emerging from the slow-moving CSM that was obscuring our line of sight during the photospheric phase. However, these broad features are challenging to identify, as they do not match the common nebular lines found in SNe (e.g. Wheeler & Benetti 2000). Few atomic species can account for both the emission lines: according to the tabulated values reported by Moore (1945), Ni I λ 6177, 7002 is a potential candidate, which would

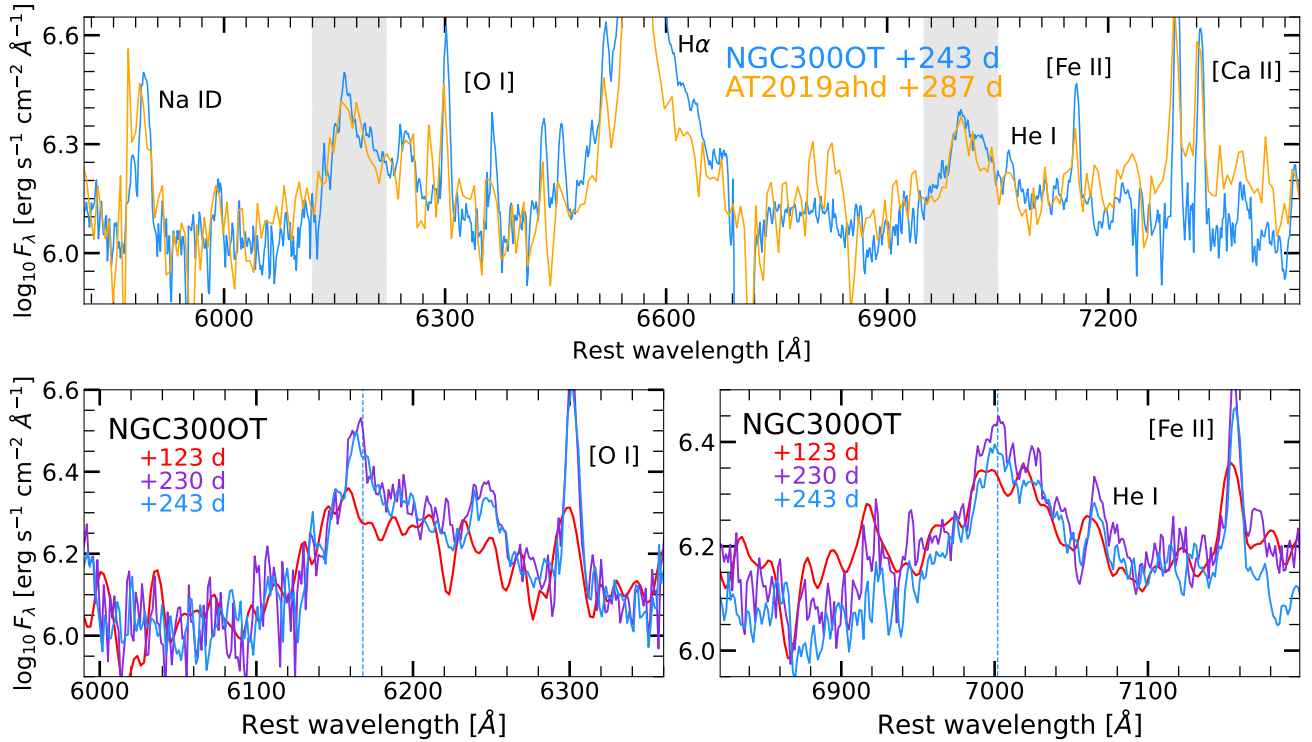


Fig. 8. Late time spectra of NGC 300 OT and AT 2019ahd. A shift in flux has been applied to superimpose the two spectra. The broad features described in the text are highlighted with grey shaded regions. The lower panels show the temporal evolution of these broad features in NGC 300 OT, starting from their first detection. Dashed vertical lines mark the positions of their peaks estimated through a Gaussian fit.

corroborate the scenario in which explosive nucleosynthesis took place during the ILRT events. In order to test this hypothesis, in Figure 9 we compare the late time spectra of NGC 300 OT and AT 2019ahd with the models of nebular spectra presented by Jerkstrand et al. (2017). The synthetic spectra have been scaled down for clarity. These models aim to reproduce the late time spectra of SNe arising from the core-collapse of a $9 M_{\odot}$ star (at zero age main sequence). The first synthetic nebular spectrum considered is relative to 300 days after explosion and has a solar abundance of elements. A high Ni content is expected to be an indicator of an ECSN event (Wanajo et al. 2009): for this reason we consider a second synthetic spectrum (again provided by Jerkstrand et al. 2017), at the same evolutionary stage, in which the ratio Ni/Fe is 30 times solar. The lower panels of Figure 9 display a zoomed-in view of the broad lines found in NGC 300 OT, together with the same spectral region of the synthetic nebular spectra. In the region of the feature peaking at $\sim 7002 \text{ \AA}$, there is a noticeable contribution in flux that is present in the Ni-rich spectrum. However, the broad emission component at 6168 \AA is not well reproduced by either synthetic spectrum, and an enhanced abundance of Ni does not seem to significantly influence this spectral region. Furthermore, a notable shortcoming of this interpretation is the lack of prominent [Ni II] lines ($\lambda\lambda 6667, 7378, 7412$, marked with dashed lines in the upper panel of Figure 9) in our ILRT spectra, which would instead be expected in the nebular spectra of a Ni-rich explosion (Jerkstrand et al. 2017). Having considered these elements, we deem it unlikely that the broad features observed originate from the nebular emission of fast, Ni-rich ejecta.

We now perform comparisons with empirical data, starting with the well-studied SN 2005cs, a low-luminosity SN IIP (Pastorello et al. 2009). The upper panel of Figure 10 shows

the nebular spectrum of SN 2005cs taken 280 days after explosion, together with the late time spectra of NGC 300 OT and AT 2019ahd. We observe a promising match for the broad feature at 6168 \AA : interestingly, during the photospheric phase of SN 2005cs there are two absorption components that are compatible with *P*-Cygni profiles in that region (bottom left panel of Figure 10). The broad emission components could therefore originate from the blend of multiple Fe II (and possibly Fe I) lines, which form a *P*-Cygni profile during the photospheric phase of SN 2005cs (+64 d), but then turn to pure emission when the continuum fades (+280 d). Subsequently, almost one year after explosion (+336 d), the broad emission component appears weakened. On the other hand, SN 2005cs does not present strong emission around the region around 7002 \AA , as shown in the bottom right panel of Figure 10, although there could arguably be a feeble *P*-Cygni profile in this region during the photospheric phase.

As a final comparison, we present the red nova V1309 Scorpii (hereby V1309 Sco, Mason et al. 2010), which is interpreted as the result of a merger of a contact binary system (Tylenda et al. 2011; Kamiński et al. 2015). The spectrum taken 48 days after the start of the outburst shows remarkable similarities to the late time spectra of our ILRTs (Figure 11). Thanks to the high resolution provided by the VLT equipped with UVES, it is possible to distinguish multiple narrow features in the spectrum of V1309 Sco which corroborates the scenario in which the broad emission components originate from the blend of multiple narrow lines. Fe I and II lines are likely candidates, although pinpointing the exact transitions involved is quite challenging. As shown in the bottom panels of Figure 11, the insurgence of this forest of emission lines is sudden, as there is no hint of emission over the continuum in the regions around 6168 \AA and 7002 \AA in the spectrum of V1309 Sco taken 26 days after the outburst.

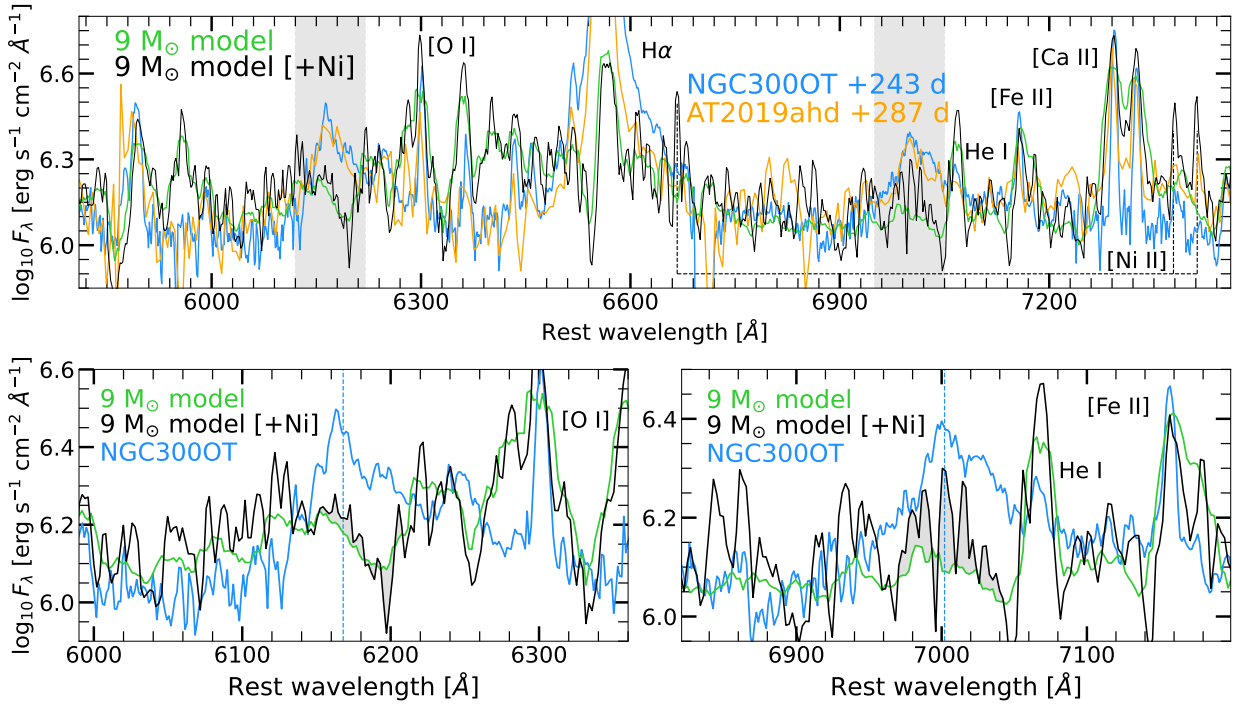


Fig. 9. Late time spectra of NGC 300 OT compared with models of nebular spectra taken from Jerkstrand et al. (2017). Forbidden [Ni II] lines expected in Ni-rich ejecta are marked with dashed lines. The bottom panels show a zoom onto the region where broad lines are observed in ILRTs. The shaded grey area in the bottom panels highlights the flux difference in the two models.

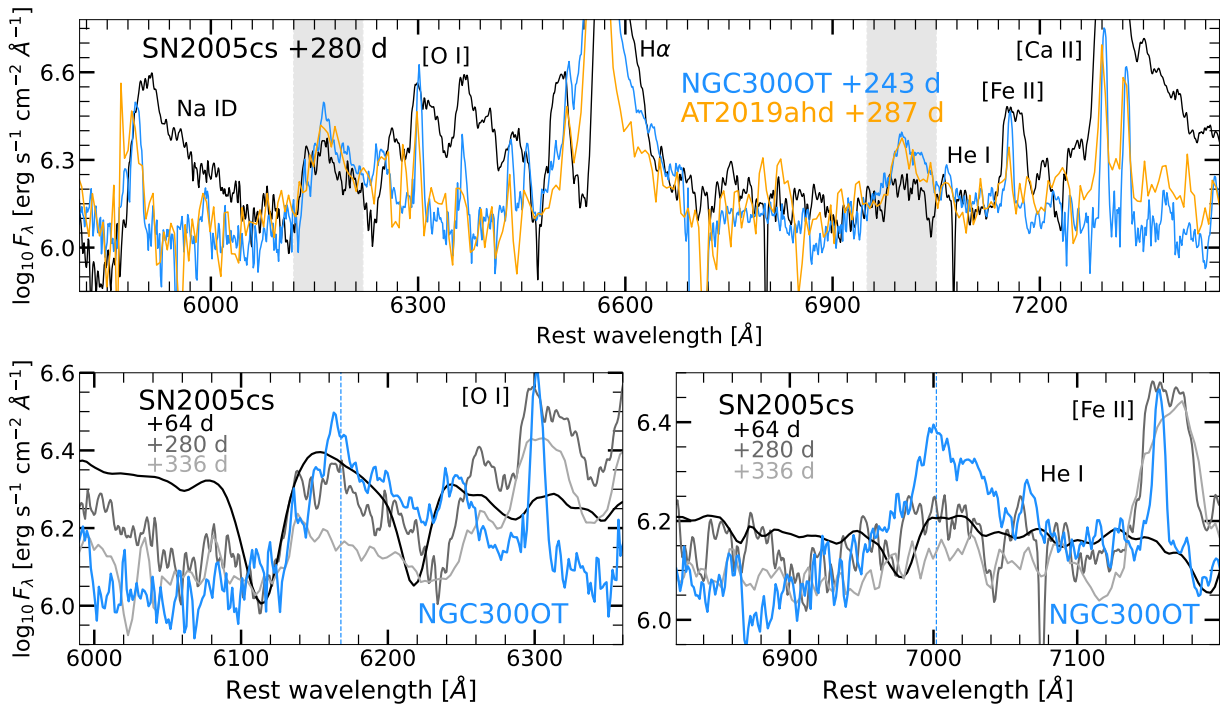


Fig. 10. Late time spectra of NGC 300 OT and AT 2019ahd compared with SN 2005cs. The lower panels show the temporal evolution of SN 2005cs in the considered wavelength ranges compared with NGC 300 OT.

Based on this comparison, we favour the interpretation that the broad emission lines observed in late time spectra of ILRTs are blends of multiple narrow (possibly Fe) lines, as observed for V1309 Sco.

This newly discovered resemblance between the spectra of V1309 Sco, AT 2019ahd and NGC 300 OT shows that emitting

regions with similar chemistry and physical conditions can be found in red novae and ILRTs. However, while there are some objects showing hybrid properties (e.g. AT 2022fnn Moran et al. 2024), this does not mean that ILRTs and LRNe can be easily blended into one class. First of all, the timescales over which V1309 Sco and the ILRTs develop these broad emission features

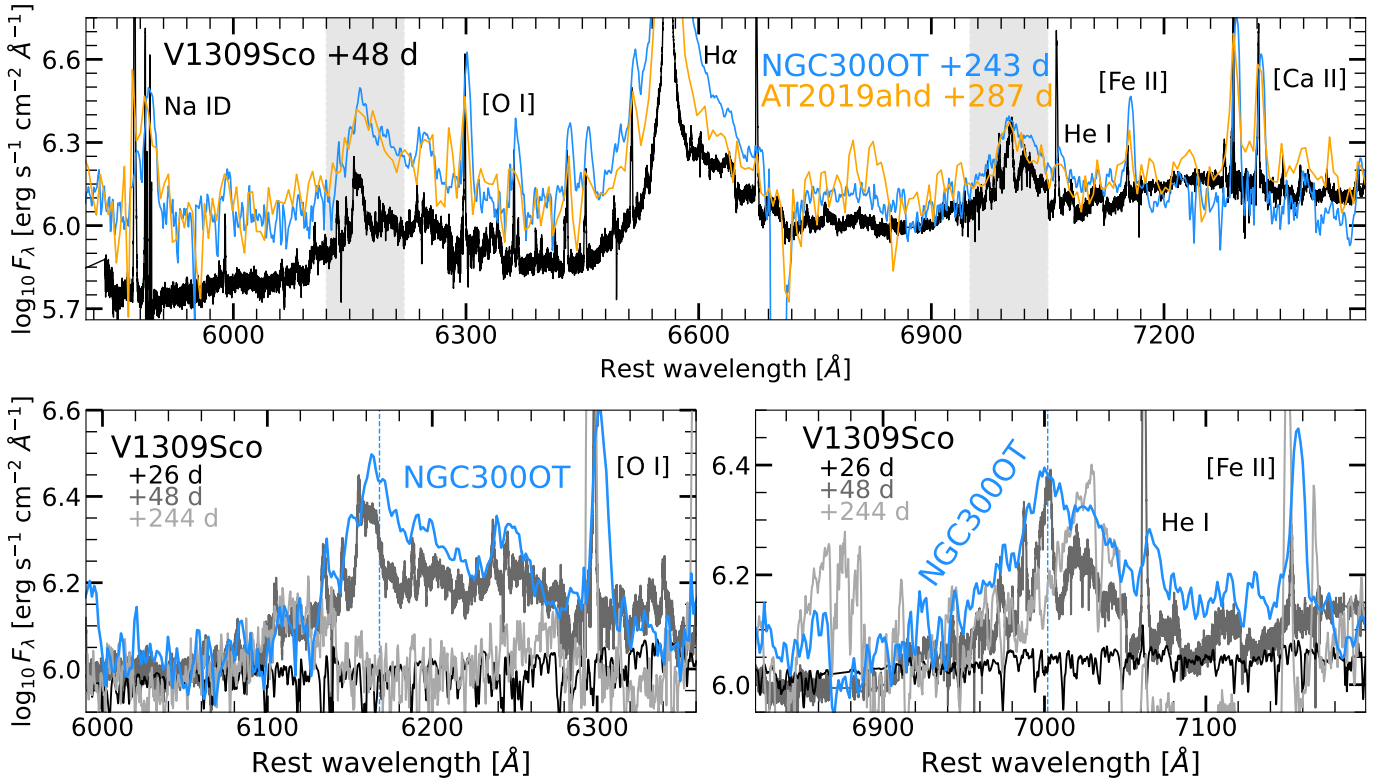


Fig. 11. Late time spectra of NGC 300 OT and AT 2019ahd compared with V1309Sco. The lower panels show the temporal evolution of V1309Sco in the considered wavelength ranges compared with NGC 300 OT.

are quite different. This could be linked to the different scale of the phenomena: the peak optical luminosity of V1309 Sco is about 150 times lower than the peak luminosity of NGC 300 OT and AT 2019ahd, and is characterised by a faster decline rate, dimming by three magnitudes in 50 days. Furthermore, late time spectra of red novae such as V1309 Sco are characterised by a red continuum eroded by the absorption of countless molecular bands, most notably TiO, VO, CO and H₂O (e.g. Goranskij et al. 2016). On the contrary, ILRTs never display the absorption features typical of molecular bands. This difference is made evident by comparing the spectrum of NGC 300 OT taken 514 days after maximum with X-Shooter with the spectrum of a red nova that already developed molecular band absorptions. Even at 514 days after maximum luminosity, the surviving continuum of NGC 300 OT does not show signs of molecular bands, which are instead prominent in the case of V1309 Sco, 244 days after the outburst (see Figure A.8).

7. The nature of ILRTs

The physical mechanism driving ILRTs has been a puzzle since the identification of this class of objects 15 years ago. We quickly outline the main observed features of these transients before reviewing some scenarios that could explain their origin:

- ILRTs present a single-peaked, monotonically declining light curve. The total radiated energy spans from a few 10^{47} to a few 10^{48} erg (Paper I).
- Whenever detected, their progenitors are heavily obscured in the optical and NIR domains, but are bright sources in the mid-infrared (MIR). These objects are associated with dust-enshrouded, extreme AGB stars in the range of 8–12 M_{\odot} (Thompson et al. 2009).

- When monitored for several years, ILRTs decline well below the progenitor level before disappearing, even in the MIR domain (Adams et al. 2016, Paper I). This favours the interpretation of ILRTs as terminal events.
- Their spectra evolve slowly and are characterised by low-excitation, narrow lines, with no signs of broad features even 17 months after discovery.

Eruption of an intermediate-mass star: One of the first scenarios proposed to explain the formation of ILRTs was the non-terminal eruption of a ~ 9 –15 M_{\odot} star, that has reached its Eddington limit and has become dynamically unstable after shedding a considerable amount of mass (Humphreys et al. 2011). The similarity between NGC 300 OT and the yellow hypergiant IRC+10420 (Bond et al. 2009; Berger et al. 2009; Humphreys et al. 2011) corroborated the idea of a stellar outburst producing an optically thick expanding envelope. However, this scenario struggles to explain the disappearance of the star observed years later in the MIR domain, as in the original view, the progenitor survives the eruption.

Stellar mergers: Thanks to the careful analysis of V1309 Sco (e.g. Tylenda et al. 2011; Mason et al. 2010), the class of transients known as red novae was soundly associated with non-degenerate stellar mergers. Depending on the masses of the progenitor stars, the peak magnitude of red novae can span from being significantly fainter than a classical nova ($M_r \sim -4.5$ mag; e.g. OGLE-2002-BLG-360, Pastorello et al. 2023) up to competing with genuine core-collapse SNe ($M_r \sim -15.5$ mag; e.g. AT 2017jfs, Tylenda et al. 2013). On the other hand, ILRTs known to date peak consistently in the range $-15 \text{ mag} \lesssim M_r \lesssim -11 \text{ mag}$ (Paper I, Cai et al. 2021). Thus, there is some overlap in the energy radiated by ILRTs and the brightest red novae: this degeneracy is worsened by the similar spectral features shown by ILRTs and red novae during their photospheric

phase. This can give rise to ambiguous objects for which a clear classification is uncertain (e.g. M85 OT2006-1, Kulkarni et al. 2007; Pastorello et al. 2007). At the same time, there are some peculiarities in these two classes of transients that help with their identification: several (although not all) red novae present a double-peaked light curve, typically weaker or absent [Ca II] emission lines, and most importantly red novae always display molecular absorption bands in their late time spectra (Pastorello & Fraser 2019), while ILRTs never show such bands. Furthermore, the progenitor systems of different red novae were observed in the optical domain (e.g. Tylenda et al. 2011; Pastorello et al. 2019), excluding the presence of large dust quantities along the line of sight, which is instead a key feature of ILRT progenitors. In principle, these differences could be tentatively explained with a different viewing angle on the same type of progenitor system (such as binary stars surrounded by a dust torus); it was indeed suggested that the same physical mechanism could power both ILRTs and red novae (e.g. Soker & Kaplan 2021). However, the expected result of a stellar merger is difficult to reconcile with the severe mid-infrared dimming observed for ILRTs over the course of a few years. Prolonged monitoring is therefore crucial to confirm the complete disappearance of the object, as there are known cases of transients settling on a lower luminosity compared to their progenitor (e.g. Beasor et al. 2024).

Failed supernovae: A hypothetical link was suggested between ILRTs and fallback supernovae, events in which a large mass fraction of the exploding star is unable to escape the gravitational potential of the compact object formed during the core-collapse (e.g. Moriya et al. 2010). Tsuna et al. (2020) found that the low energy radiated and the low photospheric temperature reached by ILRTs is compatible with radiation hydrodynamical simulations of matter ejected by a failed supernova that is interacting with pre-existing CSM. This interpretation has the merit of linking together a terminal event with the low luminosity and the narrow-line spectra of these transients. However, as noted by these latter authors, their simulations involve Wolf-Rayet and blue supergiants, which are not compatible with the progenitors of the ILRTs discovered so far. Additionally, the monitoring of NGC 300 OT and SN 2008S spanning several years has not shown signs of fallback accretion onto the black hole, which would be expected in this scenario.

Electron capture supernovae: Multiple works have proposed an association between ILRTs and ECSNe (Botticella et al. 2009; Pumo et al. 2009; Cai et al. 2018, 2021; Stritzinger et al. 2020). The 8–12 M_{\odot} extreme AGB progenitors identified by Thompson et al. (2009) are ideal candidates for giving rise to an ECSN explosion, and the intrinsic weakness of the event expected from the theory (Kitaura et al. 2006) is encouraging when considering these under-luminous objects. ILRTs, despite showing some degree of individuality, appear to be a relatively homogeneous family of objects, especially compared with the profound variability of the observable parameters within the red novae class. This can be interpreted as transients arising from similar progenitors (8–12 M_{\odot} extreme AGB stars) whose differences are caused by the interaction with different environments. The decline of the transient below the progenitor level is definitely expected in this scenario, given the terminal nature of ECSNe. In this context, the late time spectra characterised by narrow emission lines that are shown in this work merit additional comment. Type II_n SNe have shown that large quantities of CSM can bottle up the ejecta of violent stellar explosions for several years (at least 4 years in the case of SN 2015da; Tartaglia et al. 2020). Moreover, among SNe II_n it is rare to wit-

ness the emergence of the ejecta from the CSM, as observed for example for SN 1995N years after its explosion (Fransson et al. 2002; Pastorello et al. 2005). In analogy, the absence of ejecta signatures in our latest ILRT spectra does not exclude their presence underneath the CSM. The ECSN origin of these transients therefore remains a valid interpretation of the observed data, also corroborated by indirect indicators such as event rates (Cai et al. 2021, Karambelkar et al. 2023) and dust chemical composition (Rose et al. 2024).

8. Summary and conclusions

We analysed a rich collection of optical and NIR spectra of four ILRTs. Their slow evolution coupled with the presence of narrow (few 10^2 km s^{-1}) emission lines is indicative of the presence of optically thick CSM surrounding the transients. Balmer lines as well as Ca features (the Ca H&K absorption doublet, the [Ca II] doublet, and the Ca II NIR triplet) dominate the optical spectra and are recognisable at most epochs. The O I $\lambda 8446$ line appearing at late time is a consequence of the Bowen fluorescence, and could be the result of coupling between the O I $\lambda 1025.76$ line in the CSM and the Ly β line emitted by underlying ejecta. The luminosity evolution of the H emission lines and Ca II NIR triplet display a characteristic double-peaked behaviour, which is an opposing trend to that seen in neighbouring continuum flux: this is possibly linked to the interaction between fast ejecta and the slow-moving CSM.

The high-resolution spectrum of NGC 300 OT obtained with VLT + UVES shows the presence of a complex environment – which could be multiple shells of gas – causing narrow absorption features to appear on the most prominent emission lines. The characteristic shape of the [Ca II] lines is likely a result of electron scattering in an expanding medium and allows us to postulate the presence of an extended, slow ($\sim 30 \text{ km s}^{-1}$) wind surrounding the progenitor star. Late-time spectra of NGC 300 OT and AT 2019ahd display broad features never before observed in any ILRT. We find a striking similarity with the behaviour of the red nova V1309 Sco, and we tentatively explain these broad emission components as a blend of several narrow lines, possibly Fe transitions. In Paper I, we discussed how the low energy released by ILRTs coupled with their terminal nature (at the very least for NGC 300 OT) make them appealing ECSN candidates. The spectroscopic analysis performed in this work provides a characterisation of the CSM surrounding these transients: while we do not find smoking gun evidence for the explosion scenario, our findings are overall consistent with a weak ECSN event within a thick CSM.

Data availability

The spectra presented in this article, before redshift and reddening corrections, are available in WISereP:

AT 2019abn <https://www.wiserep.org/object/11956>
 AT 2019ahd <https://www.wiserep.org/object/11823>
 AT 2019udc <https://www.wiserep.org/object/13520>
 NGC 300 OT <https://www.wiserep.org/object/26452>

Acknowledgements. We thank Steve Shore and Valentina D’Orazi for the useful and lively discussions. G.V., A.P., A.R., S.B., L.T., N.E.R. and I.S. acknowledge financial support from PRIN-INAF 2022 “Shedding light on the nature of gap transients: from the observations to the models”. A.R. also acknowledges financial support from the GRAWITA Large Program Grant (PI P. D’Avanzo). Y.-Z. Cai is supported by the National Natural Science Foundation of China (NSFC, Grant No. 12303054), the Yunnan Fundamental Research Projects

(Grant No. 202401AU070063) and the International Centre of Supernovae, Yunnan Key Laboratory (No. 202302AN360001). L.G. acknowledges financial support from the Spanish Ministerio de Ciencia e Innovación (MCIN), the Agencia Estatal de Investigación (AEI) 10.13039/501100011033, and the European Social Fund (ESF). This work was funded by ANID, Millennium Science Initiative, ICN12_009 M.N. is supported by the European Research Council (ERC) under the European Union's Horizon 2020 research and innovation programme (grant agreement No. 948381). Part of the funding for GROND (both hardware as well as personnel) was generously granted from the Leibniz-Prize to Prof. G. Hasinger (DFG grant HA 1850/28-1). H.K. was funded by the Academy of Finland projects 324504 and 328898. R.K. acknowledges support from the Research Council of Finland (340613). We thank the staff of the various observatories where data were obtained for their assistance. Based on observations made with the Nordic Optical Telescope, owned in collaboration by the University of Turku and Aarhus University, and operated jointly by Aarhus University, the University of Turku and the University of Oslo, representing Denmark, Finland and Norway, the University of Iceland and Stockholm University at the Observatorio del Roque de los Muchachos, La Palma, Spain, of the Instituto de Astrofísica de Canarias. Observations from the Nordic Optical Telescope were obtained through the NUTS2 collaboration which are supported in part by the Instrument Centre for Danish Astrophysics (IDA) and the Finnish Centre for Astronomy with ESO (FINCA) via Academy of Finland grant nr 306531. The data presented here were obtained in part with ALFOSC, which is provided by the Instituto de Astrofísica de Andalucía (IAA). Time-domain research by the University of Arizona team, and D.J.S. is supported by NSF grants AST-1821987, 1813466, 1908972, 2108032, and 2308181, and by the Heising-Simons Foundation under grant #2020-1864. H.K. was funded by the Research Council of Finland projects 324504, 328898, and 353019. This work makes use of data from the Las Cumbres Observatory network. The LCO team is supported by NSF grants AST-1911225 and AST-1911151, and NASA SWIFT grant 80NSSC19K1639. Data were also obtained at the Liverpool Telescope, which is operated on the island of La Palma by Liverpool John Moores University in the Spanish Observatorio del Roque de los Muchachos with financial support from the UK Science and Technology Facilities Council. Based on observations made with the Gran Telescopio Canarias (GTC), installed in the Spanish Observatorio del Roque de los Muchachos of the Instituto de Astrofísica de Canarias, in the island of La Palma. Based on observations collected at the European Organisation for Astronomical Research in the Southern Hemisphere, Chile, as part of ePESSTO+ (the advanced Public ESO Spectroscopic Survey for Transient Objects Survey). ePESSTO+ observations were obtained under ESO program IDs 1103.D-0328 and 106.216C (PI: Ineserra). LCO data have been obtained via OPTICON. The OPTICON project has received funding from the European Union's Horizon 2020 research and innovation programme under grant no. 730890. Time domain research by the University of Arizona team and D.J.S. is supported by NSF grants AST-1821987, 1813466, 1908972, & 2108032, and by the Heising-Simons Foundation under grant #20201864.

References

- Adams, S. M., Kochanek, C. S., Prieto, J. L., et al. 2016, *MNRAS*, **460**, 1645
- Beasor, E. R., Hosseinzadeh, G., Smith, N., et al. 2024, *ApJ*, **964**, 171
- Berger, E., Soderberg, A. M., Chevalier, R. A., et al. 2009, *ApJ*, **699**, 1850
- Blinnikov, S. 2017, in *Handbook of Supernovae*, eds. A. W. Alsabti, & P. Murdin, 843
- Bond, H. E., Bedin, L. R., Bonanos, A. Z., et al. 2009, *ApJ*, **695**, L154
- Botticella, M. T., Pastorello, A., Smartt, S. J., et al. 2009, *MNRAS*, **398**, 1041
- Byrne, R. A., Fraser, M., Cai, Y. Z., Reguitti, A., & Valerin, G. 2023, *MNRAS*, **524**, 2978
- Cai, Y. Z., Pastorello, A., Fraser, M., et al. 2018, *MNRAS*, **480**, 3424
- Cai, Y. Z., Pastorello, A., Fraser, M., et al. 2021, *A&A*, **654**, A157
- Cai, Y., Reguitti, A., Valerin, G., & Wang, X. 2022, *Universe*, **8**, 493
- Callis, E., Fraser, M., Pastorello, A., et al. 2021, ArXiv e-prints [arXiv:2109.12943]
- Cardelli, J. A., Clayton, G. C., & Mathis, J. S. 1989, *ApJ*, **345**, 245
- Dekker, H., D'Odorico, S., Kaufer, A., Delabre, B., & Kotzłowski, H. 2000, in *Optical and IR Telescope Instrumentation and Detectors*, eds. M. Iye, & A. F. Moorwood, *SPIE Conf. Ser.*, **4008**, 534
- Dessart, L., Hillier, D. J., Audit, E., Livne, E., & Waldman, R. 2016, *MNRAS*, **458**, 2094
- Drake, S. A., & Ulrich, R. K. 1980, *ApJS*, **42**, 351
- Filippenko, A. V. 1997, *ARA&A*, **35**, 309
- Fransson, C., Chevalier, R. A., Filippenko, A. V., et al. 2002, *ApJ*, **572**, 350
- Fransson, C., Ergon, M., Challis, P. J., et al. 2014, *ApJ*, **797**, 118
- Goranskij, V. P., Barsukova, E. A., Spiridonova, O. I., et al. 2016, *Astrophys. Bull.*, **71**, 82
- Hiramatsu, D., Howell, D. A., Van Dyk, S. D., et al. 2021, *Nat. Astron.*, **5**, 903
- Hiramatsu, D., Tsuna, D., Berger, E., et al. 2023, *ApJ*, **955**, L8
- Holmbo, S., Stritzinger, M., Nowack, G., et al. 2019, *ATel*, **12661**, 1
- Howell, D. 2019, *Am. Astron. Soc. Meet. Abstr.*, **233**, 258.16
- Huang, C., & Chevalier, R. A. 2018, *MNRAS*, **475**, 1261
- Humphreys, R. M., & Davidson, K. 1994, *PASP*, **106**, 1025
- Humphreys, R. M., Bond, H. E., Bedin, L. R., et al. 2011, *ApJ*, **743**, 118
- Jerkstrand, A. 2017, in *Handbook of Supernovae*, eds. A. W. Alsabti, & P. Murdin, 795
- Jerkstrand, A., Ertl, T., Janka, H. T., & Müller, E. 2017, *Mem. Soc. Astron. It.*, **88**, 278
- Jha, S. W., Eweis, Y., Camacho-Neves, Y., et al. 2019, *ATel*, **12454**, 1
- Kamiński, T., Mason, E., Tylenda, R., & Schmidt, M. R. 2015, *A&A*, **580**, A34
- Karambelkar, V. R., Kasliwal, M. M., Blagorodnova, N., et al. 2023, *ApJ*, **948**, 137
- Kashi, A., Frankowski, A., & Soker, N. 2010, *ApJ*, **709**, L11
- Kiewe, M., Gal-Yam, A., Arcavi, I., et al. 2012, *ApJ*, **744**, 10
- Kitaura, F. S., Janka, H. T., & Hillebrandt, W. 2006, *A&A*, **450**, 345
- Klochkova, V. G., Yushkin, M. V., Chentsov, E. L., & Panchuk, V. E. 2002, *Astron. Rep.*, **46**, 139
- Kulkarni, S. R., Ofek, E. O., Rau, A., et al. 2007, *Nature*, **447**, 458
- Leonard, D. C., Filippenko, A. V., Barth, A. J., & Matheson, T. 2000, *ApJ*, **536**, 239
- Mason, E., & Shore, S. N. 2022, *A&A*, **664**, A12
- Mason, E., Diaz, M., Williams, R. E., Preston, G., & Bensby, T. 2010, *A&A*, **516**, A108
- Meléndez, M., Bautista, M. A., & Badnell, N. R. 2007, *A&A*, **469**, 1203
- Merrill, P. W. 1958, *Lines of the Chemical Elements in Astronomical Spectra* (Papers of the Mount Wilson Observatory, Washington: Carnegie Institution)
- Miller, A. A., Smith, N., Li, W., et al. 2010, *AJ*, **139**, 2218
- Moore, C. E. 1945, *Contrib. Princeton Univ. Obs.*, **20**, 1
- Moran, S., Kotak, R., Fraser, M., et al. 2024, *A&A*, **688**, A161
- Moriya, T., Tominaga, N., Tanaka, M., et al. 2010, *ApJ*, **719**, 1445
- Nomoto, K. 1984, *ApJ*, **277**, 791
- Osterbrock, D. E., & Ferland, G. J. 2006, *Astrophysics of Gaseous Nebulae and Active Galactic Nuclei* (Sausalito, CA: University Science Books)
- Pastorello, A., & Fraser, M. 2019, *Nat. Astron.*, **3**, 676
- Pastorello, A., Aretxaga, I., Zampieri, L., Mucciarelli, P., & Benetti, S. 2005, in 1604–2004: Supernovae as Cosmological Lighthouses, eds. M. Turatto, S. Benetti, L. Zampieri, & W. Shea, *ASP Conf. Ser.*, **342**, 285
- Pastorello, A., Della Valle, M., Smartt, S. J., et al. 2007, *Nature*, **449**, 1
- Pastorello, A., Valenti, S., Zampieri, L., et al. 2009, *MNRAS*, **394**, 2266
- Pastorello, A., Mason, E., Taubenberger, S., et al. 2019, *A&A*, **630**, A75
- Pastorello, A., Valerin, G., Fraser, M., et al. 2023, *A&A*, **671**, A158
- Patat, F., Chandra, P., Chevalier, R., et al. 2007, *Science*, **317**, 924
- Patat, F., Maund, J. R., Benetti, S., et al. 2010, *A&A*, **510**, A108
- Pumo, M. L., Turatto, M., Botticella, M. T., et al. 2009, *ApJ*, **705**, L138
- Ransome, C. L., Haberman-Mawson, S. M., Darnley, M. J., et al. 2021, *Res. Notes Am. Astron. Soc.*, **5**, 121
- Reguitti, A., Pastorello, A., Pignata, G., et al. 2022, *A&A*, **662**, L10
- Rose, S., Lau, R. M., Jenson, J. E., et al. 2024, ArXiv e-prints [arXiv:2407.20430]
- Shore, S. N., & Wahlgren, G. M. 2010, *A&A*, **515**, A108
- Smartt, S. J., Valenti, S., Fraser, M., et al. 2015, *A&A*, **579**, A40
- Smith, N. 2017, in *Handbook of Supernovae*, eds. A. W. Alsabti, & P. Murdin, 403
- Smith, N., Chornock, R., Silverman, J. M., Filippenko, A. V., & Foley, R. J. 2010, *ApJ*, **709**, 856
- Soker, N., & Kaplan, N. 2021, *Res. Astron. Astrophys.*, **21**, 090
- Stritzinger, M. D., Taddia, F., Fraser, M., et al. 2020, *A&A*, **639**, A103
- Taddia, F., Stritzinger, M. D., Sollerman, J., et al. 2013, *A&A*, **555**, A10
- Taddia, F., Stritzinger, M. D., Fransson, C., et al. 2020, *A&A*, **638**, A92
- Tartaglia, L., Pastorello, A., Sollerman, J., et al. 2020, *A&A*, **635**, A39
- Thompson, T. A., Prieto, J. L., Stanek, K. Z., et al. 2009, *ApJ*, **705**, 1364
- Tody, D. 1986, in *Instrumentation in Astronomy VI*, ed. D. L. Crawford, *SPIE Conf. Ser.*, **627**, 733
- Tody, D. 1993, in *Astronomical Data Analysis Software and Systems II*, eds. R. J. Hanisch, R. J. V. Brissenden, & J. Barnes, *ASP Conf. Ser.*, **52**, 173
- Tsuna, D., Ishii, A., Kuriyama, N., Kashiyama, K., & Shigeyama, T. 2020, *ApJ*, **897**, L44
- Tylenda, R., Hajduk, M., Kamiński, T., et al. 2011, *A&A*, **528**, A114
- Tylenda, R., Kamiński, T., Udalski, A., et al. 2013, *A&A*, **555**, A16
- Valerin, G., Pastorello, A., Reguitti, A., et al. 2025, *A&A*, **695**, A42
- Van Dyk, S. D., & Matheson, T. 2012, in *Eta Carinae and the Supernova Impostors* eds. K. Davidson, & R. M. Humphreys, *Astrophys. Space Sci. Lib.*, **384**, 249
- Ventura, P., Dell'Agli, F., Lugaro, M., et al. 2020, *A&A*, **641**, A103
- Vernet, J., Dekker, H., D'Odorico, S., et al. 2011, *A&A*, **536**, A105

- Wanajo, S., Nomoto, K., Janka, H. T., Kitaura, F. S., & Müller, B. 2009, *ApJ*, 695, 208
- Wheeler, J. C., & Benetti, S. 2000, in *Allen's Astrophysical Quantities*, ed. A. N. Cox, 451
-
- ¹ INAF – Osservatorio Astronomico di Padova, Vicolo dell'Osservatorio 5, I-35122 Padova, Italy
- ² INAF – OATS, Via G.B. Tiepolo 11, 34143 Trieste, Italy
- ³ INAF – Osservatorio Astronomico di Brera, Via E. Bianchi 46, 23807 Merate (LC), Italy
- ⁴ Yunnan Observatories, Chinese Academy of Sciences, Kunming 650216, P.R. China
- ⁵ International Centre of Supernovae, Yunnan Key Laboratory, Kunming 650216, P.R. China
- ⁶ Key Laboratory for the Structure and Evolution of Celestial Objects, Chinese Academy of Sciences, Kunming 650216, P.R. China
- ⁷ Graduate Institute of Astronomy, National Central University, 300 Jhongda Road, 32001 Jhongli, Taiwan
- ⁸ SRON, Netherlands Institute for Space Research, Niels Bohrweg 4, 2333 CA Leiden, The Netherlands
- ⁹ Department of Astrophysics/IMAPP, Radboud University Nijmegen, P.O. Box 9010, 6500 GL Nijmegen, The Netherlands
- ¹⁰ Institute of Space Sciences (ICE, CSIC), Campus UAB, Carrer de Can Magrans s/n, E-08193 Barcelona, Spain
- ¹¹ School of Physics, O'Brien Centre for Science North, University College Dublin, Belfield Dublin 4, Ireland
- ¹² The Oskar Klein Centre, Department of Astronomy, Stockholm University, AlbaNova SE-10691, Stockholm, Sweden
- ¹³ Hiroshima Astrophysical Science Center, Hiroshima University, Hiroshima, Japan
- ¹⁴ Department of Physics, Florida State University, 77 Chieftan Way, Tallahassee, FL 32306, USA
- ¹⁵ Las Cumbres Observatory, 6740 Cortona Dr. Suite 102, Goleta, CA 93117, USA
- ¹⁶ Department of Physics, University of California, Santa Barbara, CA 93106, USA
- ¹⁷ Cardiff Hub for Astrophysics Research and Technology, School of Physics & Astronomy, Cardiff University, Queens Buildings, The Parade, Cardiff CF24 3AA, UK
- ¹⁸ INAF, Osservatorio Astronomico di Capodimonte, Salita Moiarriello 16, I-80131 Napoli, Italy
- ¹⁹ DARK, Niels Bohr Institute, University of Copenhagen, Jagtvej 128, 2200 Copenhagen, Denmark
- ²⁰ Caltech/IPAC, Mailcode 100-22, Pasadena, CA 91125, USA
- ²¹ Tuorla Observatory, Department of Physics and Astronomy, University of Turku, 20014 Turku, Finland
- ²² Department of Astronomy, AlbaNova University Center, Stockholm University, SE-10691 Stockholm, Sweden
- ²³ Astrophysics Research Institute, Liverpool John Moores University, IC2, Liverpool Science Park, 146 Brownlow Hill, Liverpool L3 5RF, UK
- ²⁴ Max-Planck-Institut für Astrophysik, Karl-Schwarzschild Str. 1, D-85748 Garching, Germany
- ²⁵ Aryabhata Research Institute of Observational Sciences (ARIES), Manora Peak, Nainital 263001, India
- ²⁶ Instituto de Alta Investigación, Universidad de Tarapacá, Casilla 7D, Arica, Chile
- ²⁷ School of Physics, Trinity College Dublin, College Green, Dublin 2, Ireland
- ²⁸ Steward Observatory, University of Arizona, 933 North Cherry Avenue, Tucson, AZ 85721-0065, USA
- ²⁹ Department of Physics, University of Oxford, Keble Road, Oxford OX1 3RH, UK
- ³⁰ Astrophysics Research Centre, School of Mathematics and Physics, Queens University Belfast, Belfast BT7 1NN, UK
- ³¹ Department of Physics and Astronomy, Aarhus University, Ny Munkegade 120, DK-8000 Aarhus C, Denmark
- ³² INAF – Osservatorio Astronomico d'Abruzzo, Via M. Maggini snc, Teramo I-64100, Italy
- ³³ Department of Physics, University of California, Davis, CA 95616, USA
- ³⁴ European Southern Observatory, Alonso de Córdova 3107, Casilla 19, Santiago, Chile
- ³⁵ Millennium Institute of Astrophysics, Nuncio Monsenor Sotero Sanz 100, Providencia 8320000, Santiago, Chile
- ³⁶ INAF-Osservatorio Astrofisico di Catania, Via Santa Sofia 78, I-95123 Catania, Italy
- ³⁷ Instituto de Astrofísica, Universidad Andres Bello, Fernandez Concha 700, Las Condes, Santiago RM, Chile
- ³⁸ ICRANet, Piazza della Repubblica 10, I-65122 Pescara, Italy
- ³⁹ Institut für Theoretische Physik, Goethe Universität, Max-von-Laue-Str. 1, 60438 Frankfurt am Main, Germany
- ⁴⁰ INFN-TIFPA, Trento Institute for Fundamental Physics and Applications, Via Sommarive 14, I-38123 Trento, Italy
- ⁴¹ Institut d'Estudis Espacials de Catalunya (IEEC), E-08034 Barcelona, Spain
- ⁴² Astronomical Observatory, University of Warsaw, Al. Ujazdowskie 4, 00-478 Warszawa, Poland
- ⁴³ Center for Astrophysics, Harvard & Smithsonian, Cambridge, Massachusetts MA 02138, US
- ⁴⁴ The NSF AI Institute for Artificial Intelligence and Fundamental Interactions, 77 Massachusetts Avenue, Cambridge, USA
- ⁴⁵ Finnish Centre for Astronomy with ESO (FINCA), University of Turku, Väisäläntie 20, 21500 Piikkiö, Finland
- ⁴⁶ DTU Space, National Space Institute, Technical University of Denmark, Elektrovej 327, 2800 Kongens Lyngby, Denmark
- ⁴⁷ Istituto Nazionale di Astrofisica – Osservatorio Astronomico di Roma, Via Frascati 33, I-00040 Monteporzio Catone, Italy
- ⁴⁸ Kavli Institute for the Physics and Mathematics of the Universe (WPI), The University of Tokyo Institutes for Advanced Study, The University of Tokyo, Kashiwa, Chiba 277-8583, Japan
- ⁴⁹ INFN, Sezione di Perugia, Via A. Pascoli s/n, I-06125 Perugia, Italy
- ⁵⁰ Dipartimento di Fisica e Astronomia "G. Galilei", Università degli studi di Padova Vicolo dell'Osservatorio 3, I-35122 Padova, Italy
- ⁵¹ IAASARS, National Observatory of Athens, Metaxa & Vas. Pavlou St., 15236 Penteli, Athens, Greece
- ⁵² Department of Astronomy, University of Virginia, Charlottesville, VA 22904, USA
- ⁵³ Max-Planck-Institut für Extraterrestrische Physik, Giessenbachstraße 1, 85748 Garching, Germany
- ⁵⁴ Department of Physics and Astronomy, University of North Carolina at Chapel Hill, Chapel Hill, NC 27599, USA
- ⁵⁵ Cosmic Dawn Center (DAWN), Rådmandsgade 64, 2200 Copenhagen N., Denmark
- ⁵⁶ Niels Bohr Institute, University of Copenhagen, Jagtvej 128, 2200 København N, Denmark
- ⁵⁷ Manipal Centre for Natural Sciences, Manipal Academy of Higher Education, Manipal 576104, Karnataka, India
- ⁵⁸ Department of Physics and Astronomy, Johns Hopkins University, Baltimore, MD 21218, USA
- ⁵⁹ Space Telescope Science Institute, Baltimore, MD, USA
- ⁶⁰ Indian Institute Of Astrophysics, 100 Feet Rd, Santhosapuram, 2nd Block, Koramangala, Bengaluru, Karnataka 560034, India

Appendix A: Additional tables and figures**Table A.1.** Log of spectroscopic observations for AT 2019abn.

Date	Telescope+Instrument	Grism	Range (Å)	Res (Å)	Exp. time (s)
2019 January 26	WHT+LIRIS	HK	14000-24000	13	3840
2019 January 27	WHT+LIRIS	zJ	9000-15000	8	2160
2019 January 27	NOT+ALFOSC	gr4	3200-9600	16	1800
2019 January 29	WHT+ACAM	V400	4000-9200	14	900
2019 January 30	WHT+LIRIS	zJ	9000-15000	8	1440
2019 January 30	WHT+ACAM	V400	4000-9200	14	900
2019 February 01	WHT+ACAM	V400	4000-9200	14	900
2019 February 06	NOT+ALFOSC	gr3	4000-7000	12	2400
2019 February 11	NOT+ALFOSC	gr4	3200-9600	16	2800
2019 February 20	NOT+ALFOSC	gr4	3200-9600	12	3600
2019 February 23	NOT+ALFOSC	gr4	4000-9600	16	2400
2019 February 28	NOT+ALFOSC	gr4	3200-9600	12	2400
2019 March 02	LCO+FLOYDS	red/blue	3500-10000	13	3600
2019 March 15	NOT+ALFOSC	gr4	3200-9600	12	2700
2019 March 18	LCO+FLOYD	red/blue	3500-10000	11	3600
2019 March 23	NOT+ALFOSC	gr4	3200-9600	12	2700
2019 March 29	LCO+FLOYD	red/blue	3500-10000	13	3600
2019 April 04	CAHA+PMAS	–	4500-7300	9	600
2019 April 09	LCO+FLOYD	red/blue	3500-10000	13	3600
2019 April 23	NOT+ALFOSC	gr4	3200-9600	12	1800
2019 May 09	LCO+FLOYD	red/blue	3500-10000	13	3600
2019 May 15	NOT+ALFOSC	gr4	3200-9600	15	3600
2019 May 20	LCO+FLOYD	red/blue	3500-10000	11	3600
2019 June 04	NOT+ALFOSC	gr4	3200-9600	14	3600
2019 June 22	LCO+FLOYD	red/blue	3500-10000	13	3600
2019 July 20	NOT+ALFOSC	gr4	3200-9600	12	3600
2019 July 26	LCO+FLOYD	red/blue	3500-10000	12	3600
2019 August 20	NOT+ALFOSC	gr4	3200-9600	15	3600
2019 August 30	NOT+ALFOSC	gr4	3200-9600	12	3600

Table A.2. Log of spectroscopic observations for AT 2019ahd.

Date	Telescope+Instrument	Grism	Range (Å)	Res (Å)	Exp. time (s)
2019 January 30	SALT+RSS	PG0900	3500-9300	5	1890
2019 February 01	WHT+ACAM	V400	4000-9200	11	1800
2019 February 06	NOT+ALFOSC	gr4	3200-9600	12	3600
2019 February 11	NOT+ALFOSC	gr4	3200-9600	16	3600
2019 February 28	NOT+ALFOSC	gr4	3200-9600	12	3600
2019 March 05	SALT+RSS	PG0700	3500-9300	16	1800
2019 March 15	NOT+ALFOSC	gr4	3200-9600	12	2700
2019 April 07	NOT+ALFOSC	gr4	3200-9600	12	3000
2019 April 18	NOT+ALFOSC	gr4	3200-9600	12	3600
2019 May 14	NOT+ALFOSC	gr4	3200-9600	12	3600
2019 May 21	SALT+RSS	PG0700	3500-9300	15	1800
2019 November 23	GTC+OSIRIS	R1000R	5100-10300	6	1350

Table A.3. Log of spectroscopic observations for AT 2019udc.

Date	Telescope+Instrument	Grism	Range (Å)	Res (Å)	Exp. time (s)
2019 November 04	LCO+FLOYDS	red/blue	3500-10000	12	2700
2019 November 04	HCT-HFOSC2	gr7	4000-7600	18	1800
2019 November 05	HCT-HFOSC2	gr7	4000-7600	18	2700
2019 November 06	LCO+FLOYDS	red/blue	3500-10000	18	2700
2019 November 13	LCO+FLOYDS	red/blue	3500-10000	12	3600
2019 November 14	LCO+FLOYDS	red/blue	3500-10000	12	3600
2019 November 15	LCO+FLOYDS	red/blue	3500-10000	16	3600
2019 November 17	LCO+FLOYDS	red/blue	3500-10000	12	3600
2019 November 18	LCO+FLOYDS	red/blue	3500-10000	15	3600
2019 November 22	GTC+OSIRIS	R1000R+B	3600-10300	7	1380
2019 November 30	LCO+FLOYDS	red/blue	3500-10000	12	3600
2019 December 03	LCO+FLOYDS	red/blue	3500-10000	12	3600
2019 December 06	Baade+FIRE	prism	8000-22000	30	888
2019 December 14	NOT+ALFOSC	gr4	3200-9600	20	2800
2019 December 24	LCO+FLOYDS	red/blue	3500-10000	13	3600
2019 December 29	NTT+EFOSC2	gr20	6000-7100	13	2400
2020 January 19	LCO+FLOYDS	red/blue	3500-10000	12	3600

Table A.4. Log of spectroscopic observations for NGC 300 OT. FORS spectra were taken from [Patat et al. \(2010\)](#).

Date	Telescope+Instrument	Grism	Range (Å)	Res (Å)	Exp. time (s)
2008 May 16	BMagellan+IMACShort	g200	4000-10500	6	100x2
2008 May 30	DuPont+B&C	g300	3500-9600	8	300
2008 June 04	DuPont+B&C	g300	3500-9600	8	300
2008 June 06	NTT+EFOSC	gm3-gm5	3300-9200	B11 R15	1460x2
2008 June 11	CMagellan+LDSS3	-	3700-9800	4	300x3
2008 June 13	NTT+EFOSC	gm3-gm5	3300-9200	B11 R15	1460x2
2008 June 15	NTT+EFOSC	gm3-gm5	3300-9200	B11 R15	1460x2
2008 June 16	BMagellan+IMACSlong	g300	3700-7900	4	300x3
2008 July 01	VLT+FORs	300V	3300-9200	11	1800
2008 July 02	VLT+UVES	SHP700+HER_5	3400-8000	B0.12 R0.36	1500x6
2008 July 05	NTT+EFOSC	gm3-gm5	3300-9200	B11 R15	1460x2
2008 July 08	VLT+FORs	300V	3300-9200	11	2160
2008 July 15	NTT+EFOSC	gm3-gm5	3300-9200	B11 R15	1460x2
2008 July 23	CTIO4m+R-CSpec	KPGL3-1	4000-7600	5	720
2008 July 24	CTIO4m+R-CSpec	KPGL3-1	4000-7600	5	1200
2008 July 25	CTIO4m+R-CSpec	KPGL3-1	4000-7600	5	1200
2008 August 05	NTT+EFOSC	gm3-gm5	3300-9200	B11 R15	1460x2
2008 September 17	CMagellan+LDSS3	VPH-All	3700-9400	6	900
2008 October 02	Palomar200i+DBSP	300/3990+158/7500	3300-10300	B11 R16	1800x2
2008 October 08	TNG+NICS	IJHK	8700-24700	IJH16 K30	-
2008 October 14	WHT+ISIS	R158R+R300B	3400-10200	B4 R6	600x3
2009 January 07	Gemini South+GMOS	-	4000-8000	6	1580
2009 January 21	Gemini South+GMOS	-	4000-8000	6	1800
2009 October 12	VLT+X-Shooter	-	5600-24400	B0.7 R2.7	300

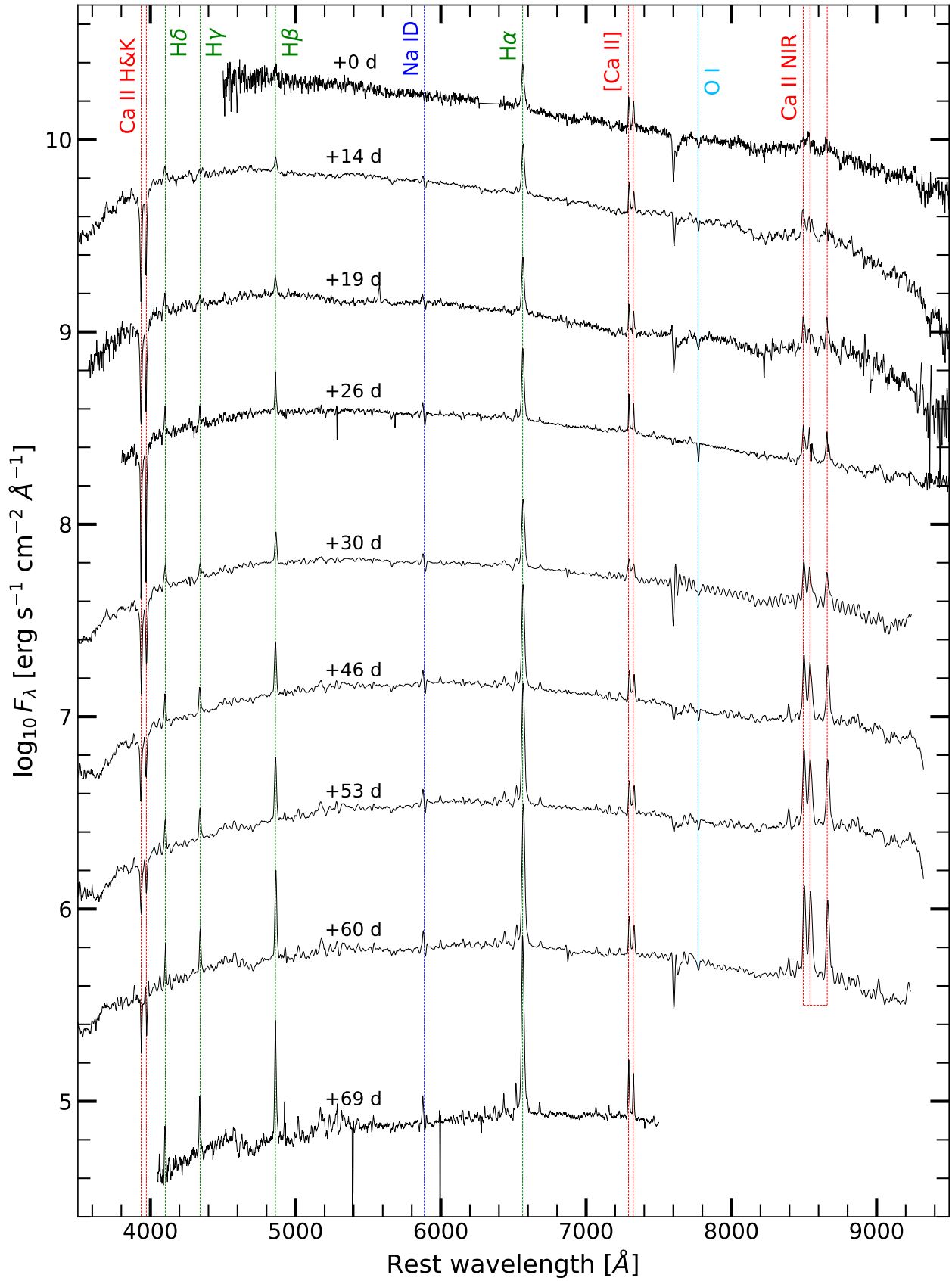


Fig. A.1. NGC 300 OT spectra during the early phases. Ca lines are highlighted in red, H lines in green, O lines in light blue and the Na ID absorption doublet in blue. Epochs are reported with respect to maximum r band luminosity.

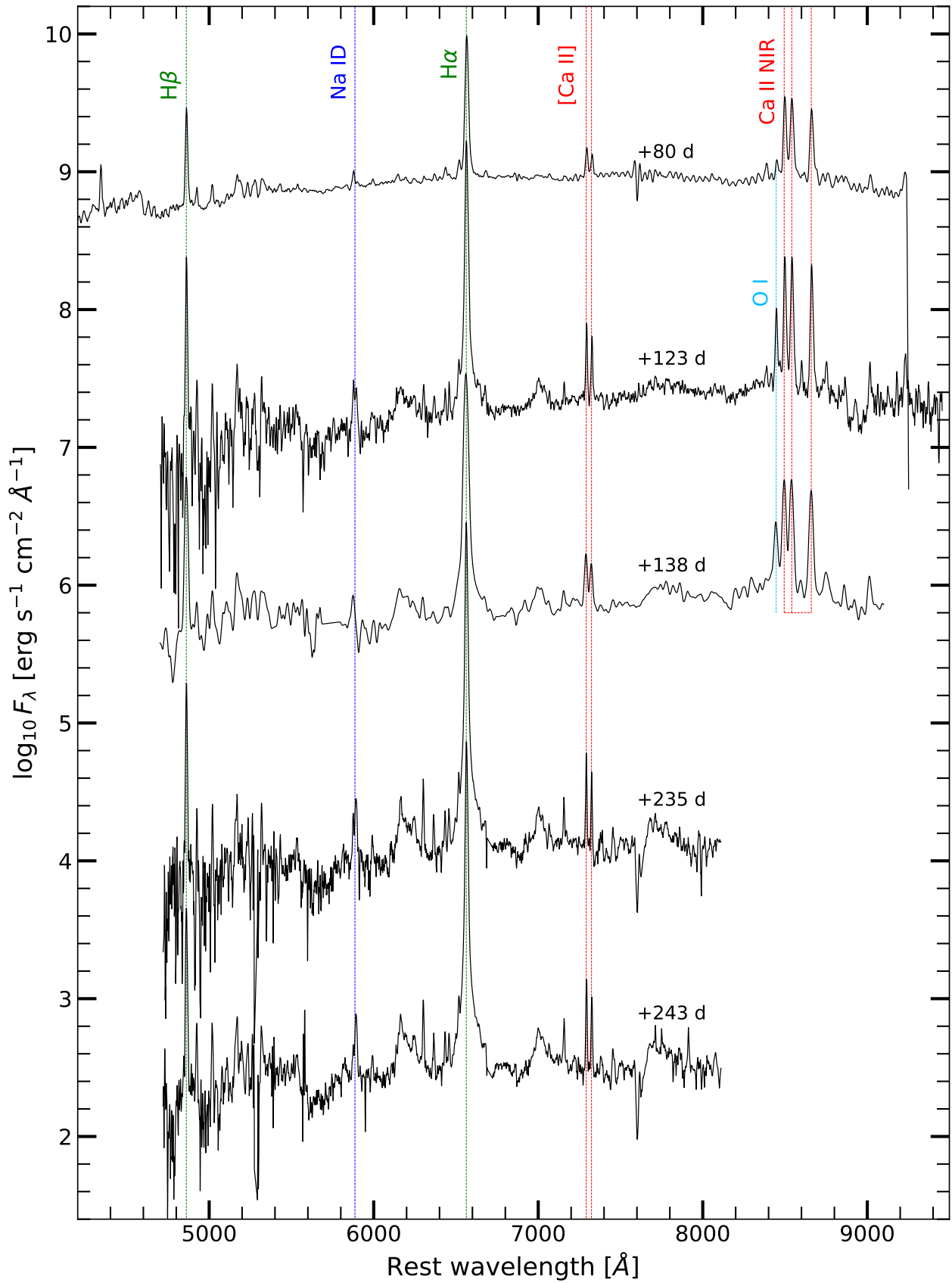


Fig. A.2. NGC 300 OT spectra during the late phases of its evolution. Ca lines are highlighted in red, H lines in green, O lines in light blue and the Na ID absorption doublet in blue. Epochs are reported with respect to maximum r band luminosity.

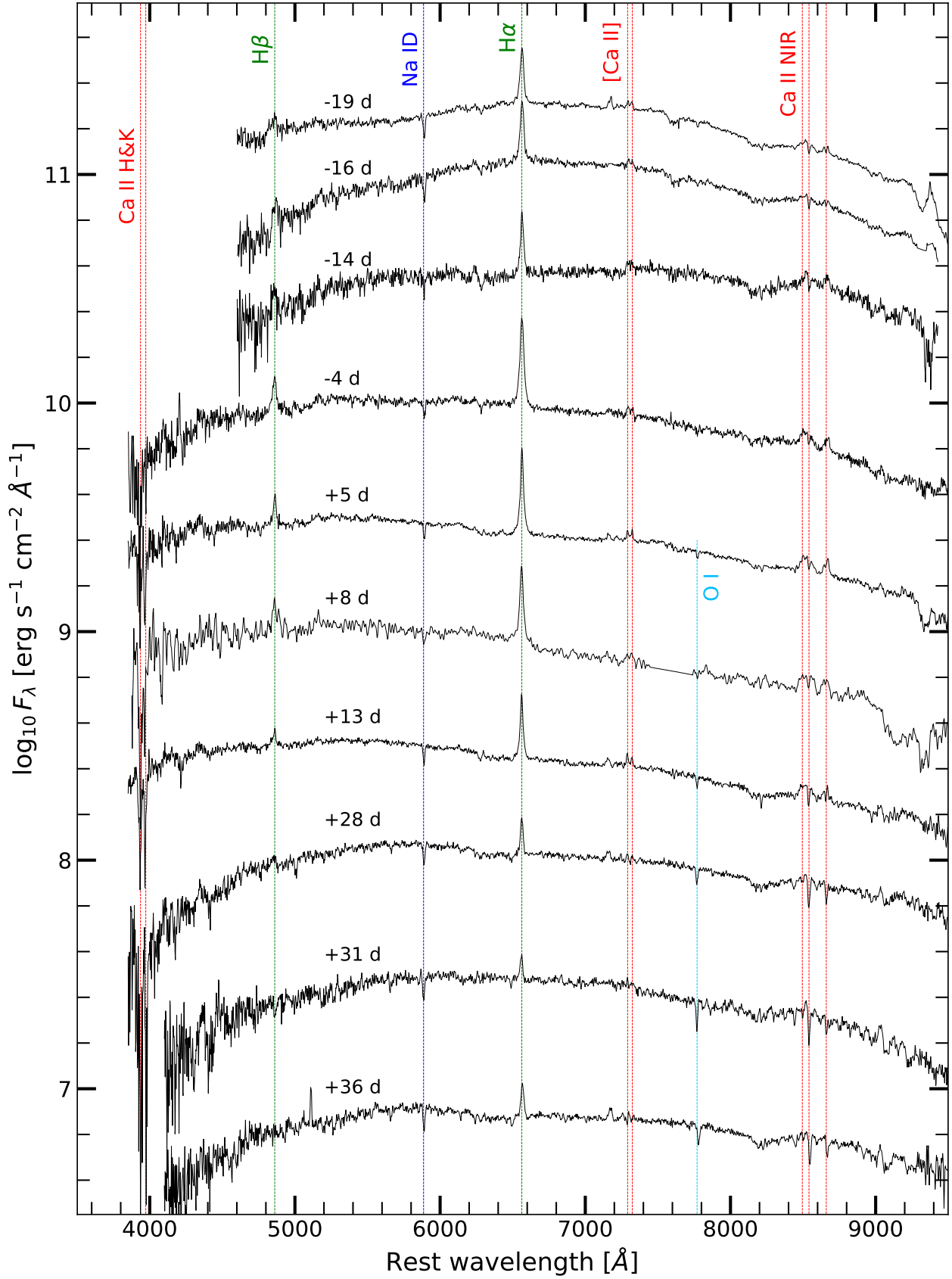


Fig. A.3. AT2019abn spectra collected in the early phases. Ca lines are highlighted in red, H lines in green, O lines in light blue and the Na ID absorption doublet in blue. Epochs are reported with respect to maximum *r* band luminosity.

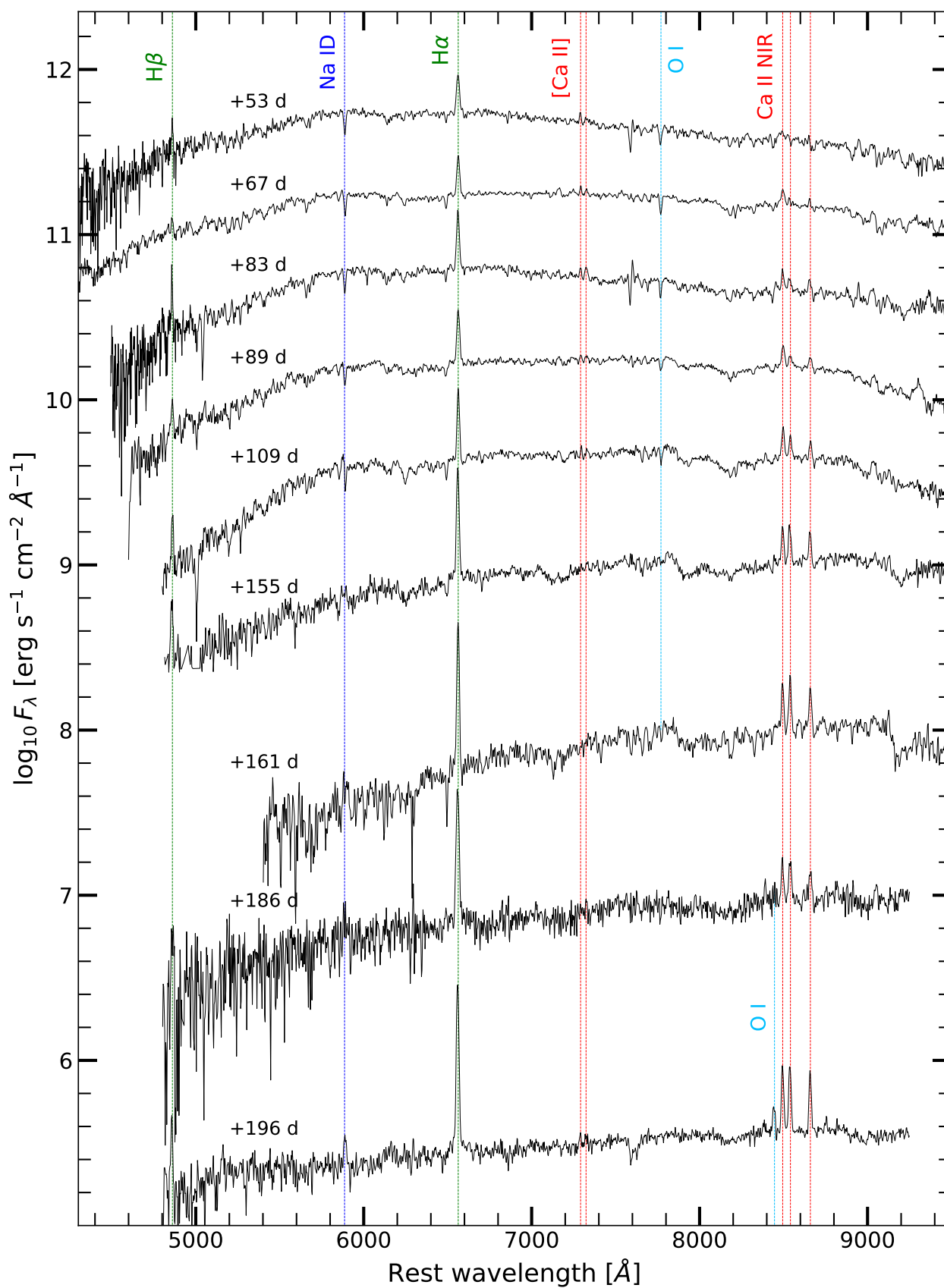


Fig. A.4. AT2019abn late spectra. Ca lines are highlighted in red, H lines in green, O lines in light blue and the Na ID absorption doublet in blue. Epochs are reported with respect to maximum r band luminosity.

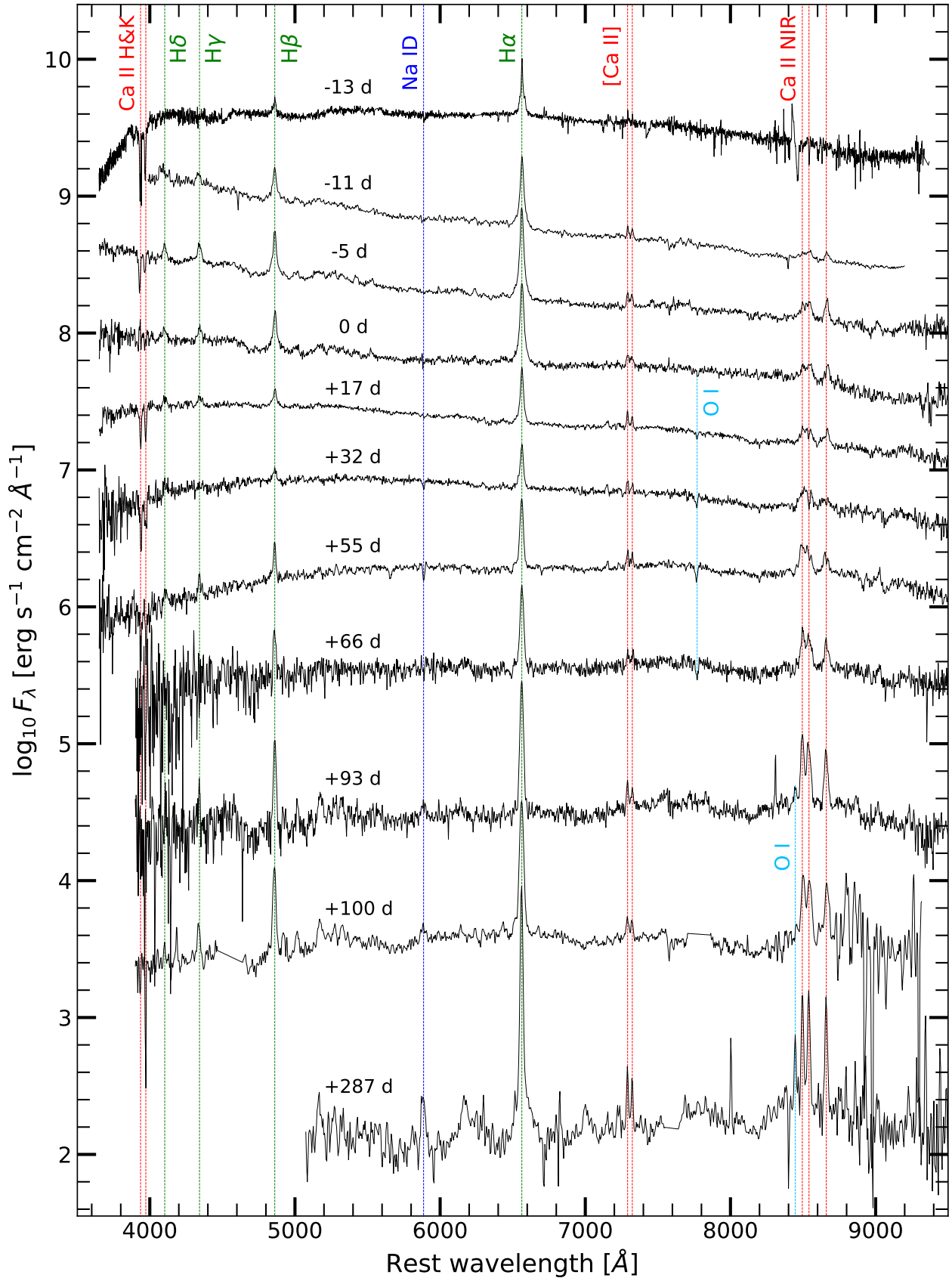


Fig. A.5. Spectra of AT2019ahd. Ca lines are highlighted in red, H lines in green, O lines in light blue and the Na ID absorption doublet in blue. Epochs are reported with respect to maximum *r* band luminosity.

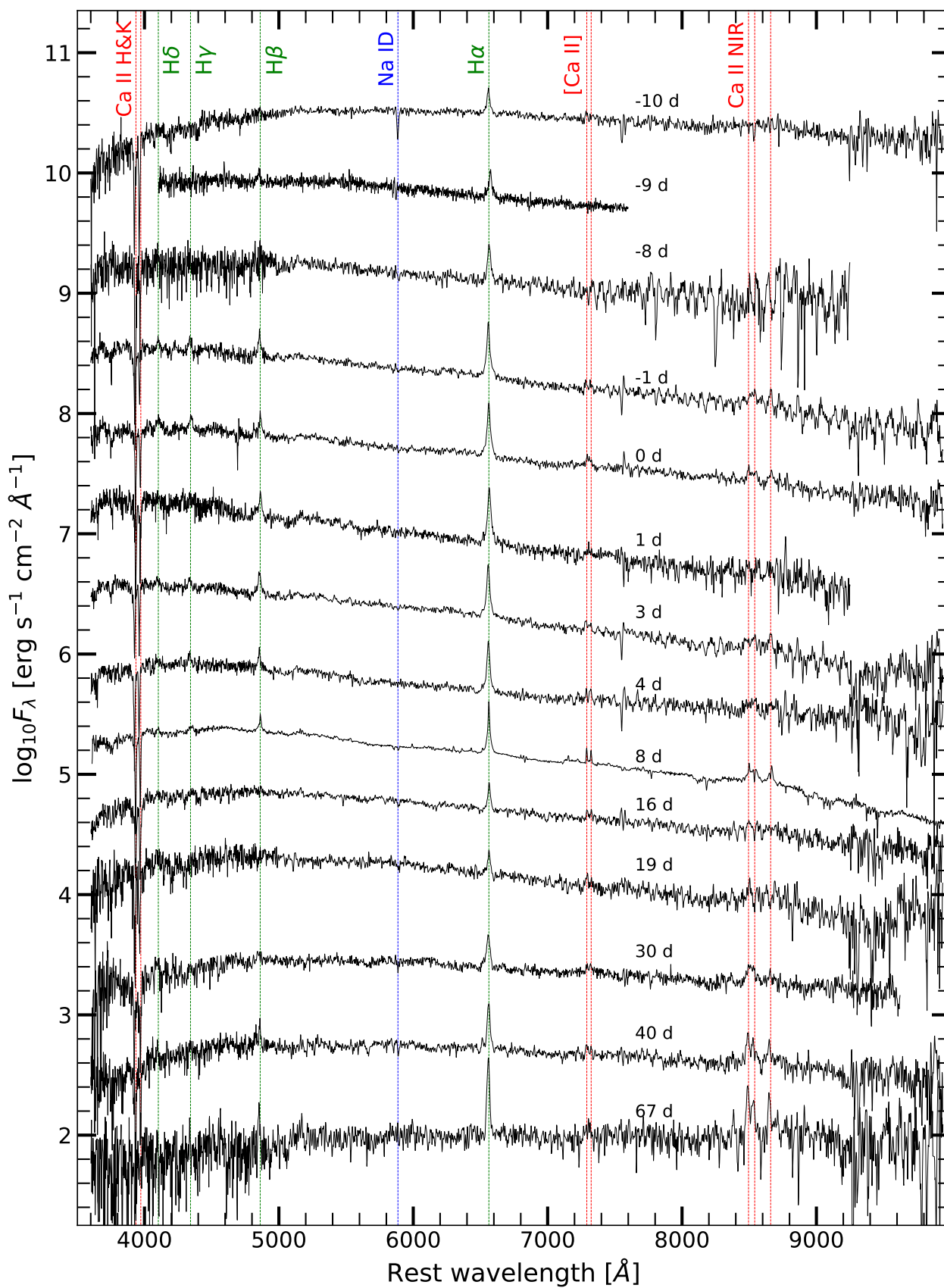


Fig. A.6. Spectra collected for AT2019udc. Ca lines are highlighted in red, H lines in green and, O lines in light blue the Na ID absorption doublet in blue. Epochs are reported with respect to maximum r band luminosity.

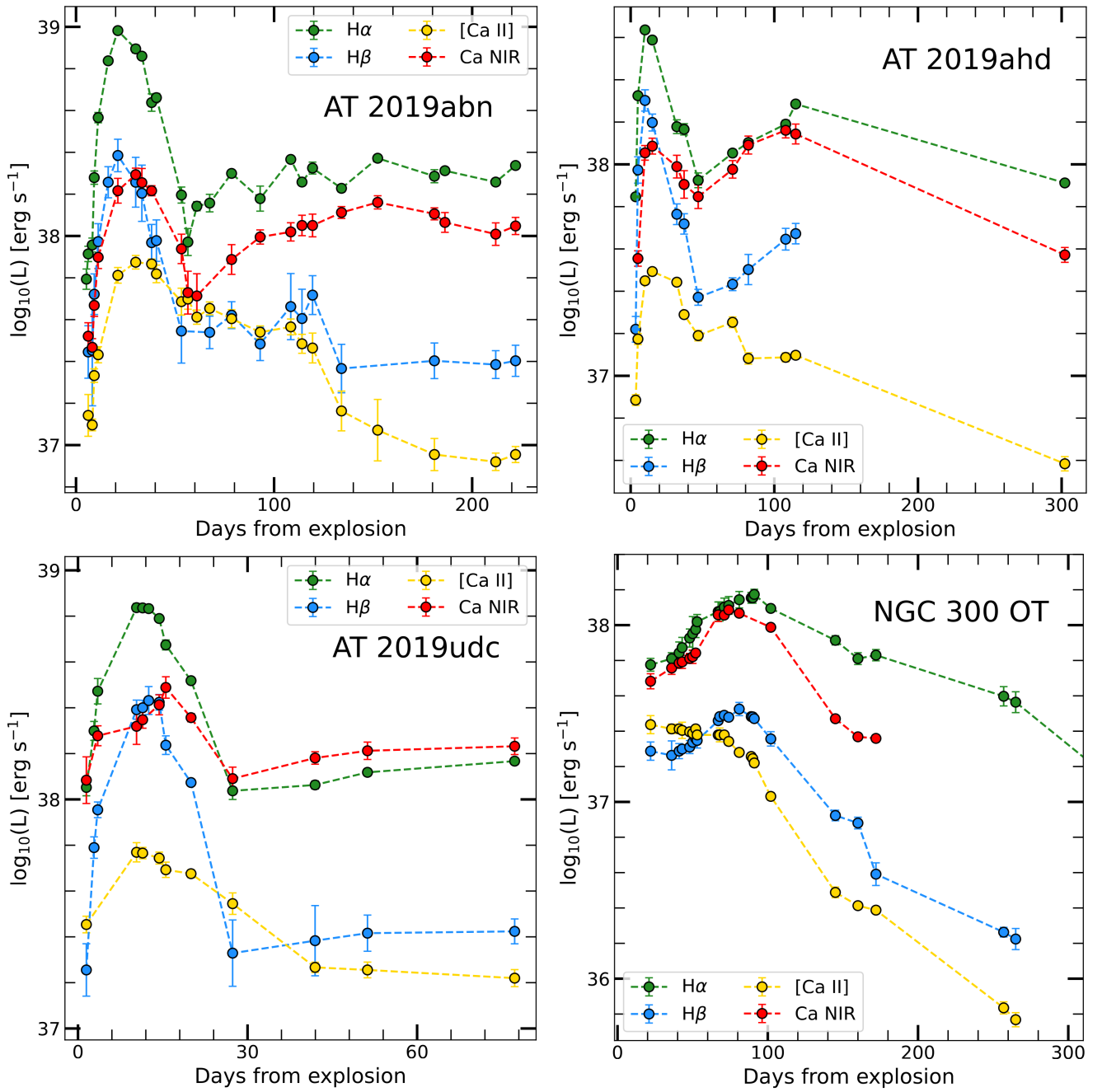


Fig. A.7. Luminosity of the emission lines for our sample of ILRTs, grouped by transient rather than by emission feature (as in Figure 3).

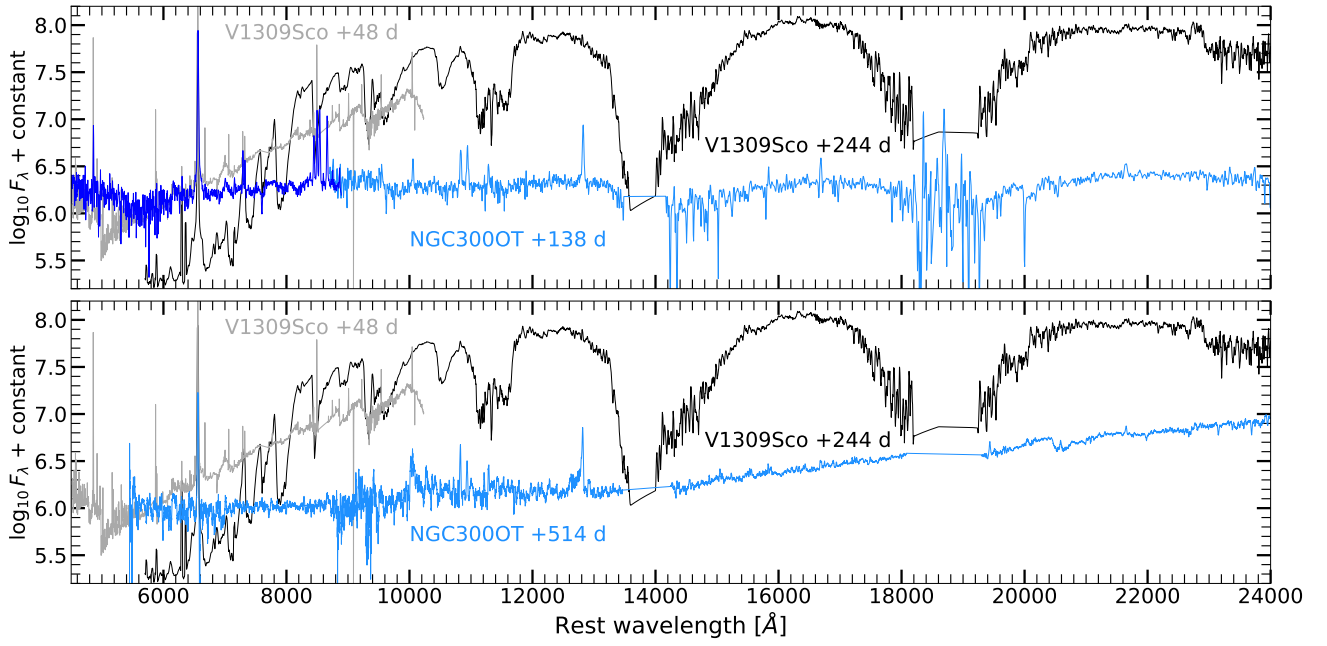


Fig. A.8. Late time NIR spectra of NGC 300 OT compared with V 1309 Sco. In the upper panel, the NIR spectrum of NGC 300 OT taken with TNG+NICS on 2008 October 08 (shown in light blue) is plotted along with the optical spectrum obtained with WHT+ISIS six days later (in blue). For a more detailed spectroscopic evolution of V1309 Sco see [Kamiński et al. 2015](#).